Journal of Electronic Materials
https://doi.org/10.1007/s11664-026-12965-0

ORIGINAL RESEARCH ARTICLE

Composition-Dependent Electrochemical Performance of rGO-MnO_2-PPy Nanocomposites in Acidic and Neutral Electrolytes

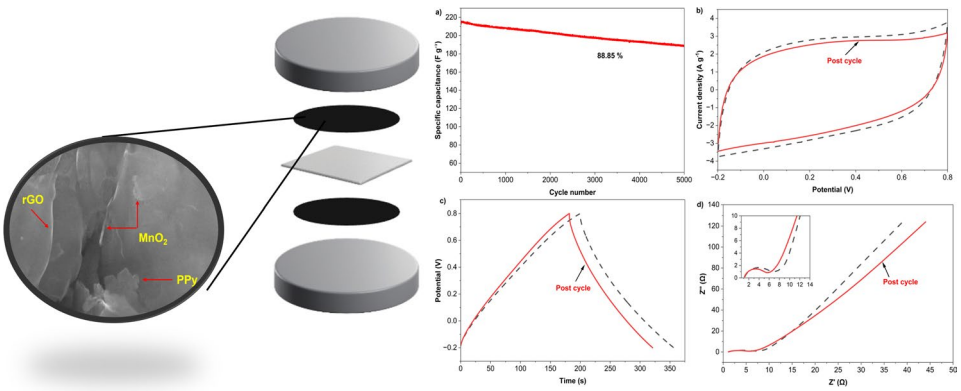
Beray Alyakut[1] · Zafer Çıplak[2] · Nuray Yıldız[3]

Received: 2 February 2026 / Accepted: 23 May 2026
© The Author(s) 2026

Abstract

The demand for supercapacitor electrode materials with high specific capacitance, enhanced energy density, and superior power capability continues to increase. In addition to superior capacitance, electrode materials are required to deliver high energy density, cycling stability, and rate capability. In this study, we produced a rGO-MnO_2-PPy nanocomposite using a facile two-step method. First, rGO-MnO_2 was produced by hydrothermal synthesis. Subsequently, the rGO-MnO_2-PPy nanocomposite was obtained through the polymerization and coating of polypyrrole (PPy) on the rGO-MnO_2 surface. The electrochemical characterization of the electrodes was carried out in both Na_2SO_4 and acidic H_2SO_4 electrolytes using a two-electrode configuration. Benefiting from the synergistic interaction among its constituents, the nanocomposite exhibited specific capacitance of 345.87 and 220.16 F g^{-1} at 0.5 A g^{-1} in 0.5 M Na_2SO_4 and 1 M H_2SO_4 electrolytes, respectively. In addition, the ternary nanocomposite electrode exhibited good rate capability, retaining 81.03% and 72.03% of its specific capacitance over a current density range of 0.5–5 A g^{-1} in 0.5 M Na_2SO_4 and 1 M H_2SO_4 electrolytes, respectively. After 5000 galvanostatic charge–discharge cycles, the electrode showed excellent cycling stability, maintaining 88.85% and 86.08% of its initial capacitance in 0.5 M Na_2SO_4 and 1 M H_2SO_4 electrolytes, respectively. The rGO-MnO_2-PPy nanocomposite symmetric cell delivered power density of 1421.97 W kg^{-1} and energy density of 8.65 Wh kg^{-1}, highlighting its promise as an electrode material for next-generation supercapacitors.

Graphical Abstract



Keywords Supercapacitor · reduced graphene oxide · polypyrrole · nanocomposite

Introduction

Energy demand is increasing with the growing population. Fossil fuels have traditionally been the preferred choice for supplying the growing demand for energy. However,

Extended author information available on the last page of the article

Published online: 11 June 2026

the use of fossil fuels leads to greenhouse gas emissions, which contributes to environmental pollution, one of the world's most significant problems. For this reason, environmentally friendly and sustainable energy sources are required.[1,2] Renewable energy sources such as wind and solar, by their very nature, can be affected by weather conditions, leading to voltage and frequency fluctuations. This situation can result in imbalances between generated and demanded power, as well as potential damage to sensitive equipment.[3,4] To ensure that these systems contribute to continuous and stable energy production, their integration with different power systems is essential for efficient and balanced energy generation. Supercapacitors can be integrated into power grids to maintain balance in energy production and manage power quality. They help reduce high-frequency power fluctuations caused by renewable energy sources by responding quickly.[5,6] Supercapacitors are generally used in hybrid systems or in conjunction with power conversion techniques that increase efficiency and expand their range of applications.[7–10] For this reason, supercapacitors have attracted increasing interest owing to their advantageous functional properties in energy storage technologies, including higher energy density, rapid charge–discharge capability, and extended operational lifespan. In contrast to conventional battery systems, supercapacitors are capable of supplying high power output within brief time intervals, which makes them suitable for use in electric vehicles, portable electronic devices, backup power systems, and various renewable energy applications. Depending on their fundamental charge-storage mechanism, supercapacitor electrodes are generally categorized as electric double-layer capacitors (EDLC) or pseudocapacitors.[11]

In EDLCs, charge accumulation arises from the establishment of an electrostatic double layer at the interface separating the electrolyte from the electrode surface.[12] These devices typically store charge through physical adsorption processes. As a result, EDLCs commonly exhibit high power capability and outstanding cycle durability but relatively low energy density, as the storage mechanism is purely electrostatic. The electrode structures utilized in these systems are capable of sustaining prolonged charge–discharge cycling with negligible deterioration in electrochemical performance.[13] Consequently, carbonaceous materials such as activated carbon, carbon nanotubes (CNTs), and graphene-derived structures, which offer large specific surface area and tunable pore characteristics, are frequently selected as electrode candidates for EDLC applications.[14,15]

Graphene-based electrode materials are particularly attractive because of their large surface area for electrostatic charge storage, high specific capacitance, excellent electrical conductivity, long cycle life, and mechanical stability.[16,17] Among them, graphene oxide (GO) and reduced graphene oxide (rGO) are popular graphene-based materials. rGO exhibits several electrochemical properties that make it more advantageous than GO for supercapacitor applications. The reduction of GO to rGO enhances its electrical conductivity, charge-transfer kinetics, and capacitive properties, thereby rendering rGO a more promising electrode candidate for energy storage systems.[18,19] Pseudocapacitive electrode materials, on the other hand, store charge through fast redox reactions occurring at/near the electrode surface or through rapid ion addition/de-intercalation into the layered structure of the electrode material.[20,21] Therefore, pseudocapacitors exhibit greater specific capacitance and enhanced energy density relative to EDLCs, which are constrained by limited ion adsorption and purely electrostatic charge-storage behavior.[13,22] The electrode materials used in pseudocapacitors consist of redox-active components, including metal oxides, metal-doped carbon materials, and conductive polymers.[23,24] Among transition metal oxides, RuO_2, Co_3O_4, V_2O_5, and MnO_2 are commonly used in pseudocapacitors, offering high theoretical specific capacitance and energy density.[25] MnO_2 is commonly favored because it is inexpensive, widely available, and environmentally benign. However, its limited electrical conductivity, structural deterioration occurring throughout charge–discharge cycling, and the leaching of Mn in acidic electrolytes restrict its electrochemical performance.[25–27] Another widely investigated pseudocapacitive material is polypyrrole (PPy), a conducting polymer that is regarded as an effective electrode component owing to its straightforward synthesis, good electrical conductivity, notable environmental and thermal robustness, and substantial theoretical capacitance (~3400 F g^{-1}).[28–30] However, a common issue with conducting polymers is the structural deformation arising from the expansion and contraction of polymer chains under prolonged charge–discharge cycling. This leads to increased resistance, decreased capacitance, and reduced rate capability.[28,30,31]

A particularly desirable characteristic of supercapacitor electrodes is their extended lifespan. Over time, factors such as pore clogging in the electrode material, chemical instability, and corrosion of current collectors lead to the degradation and aging of supercapacitors. Understanding these mechanisms requires strategies to improve electrochemical performance. On the other hand, the lower energy density of supercapacitors compared to batteries poses a challenge in the field of energy storage as it limits their use in applications that require both high energy and high power densities.[32] To overcome these disadvantages, a synergistic effect can be created by combining pseudocapacitance and EDLC materials. In such systems, rGO provides a conductive and stable framework with its high surface area and good charge transfer properties, while metal oxides/conducting polymers contribute to high specific capacitance and energy density. This synergistic effect yields electrode materials with long cycle life, electrochemical stability, and high energy storage

performance in supercapacitor applications.[33] Studies based on electrode materials comprising rGO, MnO_2, and PPy clearly demonstrate the potential of these materials for supercapacitor applications. Previous research has reported rGO-MnO_2-PPy nanocomposites prepared via various synthesis routes and exhibiting diverse morphological features, including polymerization of pyrrole microwave-reduced rGO-MnO_2,[34] electrodeposition of PPy,[35] electrodeposition of PPy and MnO_2 into rGO aerogel,[36] co-assembly of MnO_2-GO and PPy-GO with ultrasonication,[37] filtration-directed self-assembly of rGO, MnO_2, and PPy,[38] PPy decoration of rGO-MnO_2 on the CNT surface,[39] and MnO_2 deposition on graphene foam@PPy,[40] which have attracted considerable attention in the field. The combined use of rGO, MnO_2, and PPy creates a synergistic effect through the combined contribution of conductivity, pseudocapacitance, and structural stability, which has a positive effect on specific capacitance and significantly improves electrochemical performance. However, the effective utilization of such hybrid systems is still needed in order to overcome intrinsic limitations of each component, maximizing synergistic effects and achieving optimal electrochemical performance. Among the various factors influencing the performance of such electrode materials, the nanocomposite composition plays a crucial role in determining the physicochemical properties and, consequently, the electrochemical behavior. Therefore, in this study, particular emphasis is placed on systematically investigating the effect of nanocomposite composition on the electrochemical performance of a ternary rGO–MnO_2–PPy nanocomposite.

Electrolytes significantly affect supercapacitor behavior by governing parameters such as capacitance, energy density, and operational stability. In particular, aqueous electrolyte systems provide superior ionic conductivity, which can contribute to improved electrochemical performance.[41] Among them, acidic electrolytes, which are a type of aqueous electrolyte, can cause surface dissolution or structural degradation when contacted with chemically unstable electrode materials. Over time, this reduces the electrode's performance and shortens its lifespan. Neutral electrolytes have a lower corrosive effect on the material; however, due to the lower mobility of ions such as Na^+ and K^+ in the electrode–electrolyte interactions, they can hinder charge–discharge rates, negatively affecting the formation of the electric double layer and, consequently, the capacity.[8–10] Acidic electrolytes, particularly H_2SO_4, are widely used due to their high ionic conductivity (~0.8 S cm^{-1} at 25°C), whereas neutral electrolytes, such as Li_2SO_4, Na_2SO_4, and K_2SO_4, offer wider voltage windows and lower corrosivity. Notably, Na_2SO_4 is especially effective for MnO_2-based pseudocapacitive materials. Performance largely depends on the interaction between ion size and electrode material. The favorable ionic radius of Na^+ in the Na_2SO_4 electrolyte promotes efficient ion diffusion and facilitates rapid adsorption–desorption processes on the MnO_2 surface. This feature is particularly beneficial for porous and hierarchical MnO_2 architectures, where the appropriate ion size enables accelerated mass transport and effective utilization of the active material.[10,42,43] For this reason, the development of electrodes capable of operating in both neutral and acidic electrolytes provides flexibility in terms of application and enables operation over a wider potential range; however, this requires the selection of appropriate materials. Operation in different pH environments can affect the energy density and stability of supercapacitors. Although carbon-based supercapacitors demonstrate higher capacitance in acidic electrolytes, studies have shown that energy density can be enhanced by optimizing the operating potential window under neutral electrolyte conditions.[9,44,45]

In this study, we produced rGO-MnO_2-PPy nanocomposites by *in situ* polymerization of pyrrole on the surface of hydrothermally synthesized rGO-MnO_2. Additionally, by varying the amounts of $KMnO_4$ and pyrrole during electrode material fabrication, nanocomposites with different MnO_2 and PPy compositions were obtained, and their electrochemical properties were systematically investigated. The proposed strategy offers a novel and effective approach for compositional engineering of rGO-MnO_2-PPy nanocomposites, leading to a deeper understanding of structure–property relationships in supercapacitor electrodes. Moreover, electrochemical performance of rGO-MnO_2-PPy nanocomposites was evaluated in both acidic and neutral electrolytes applying a symmetric two-electrode configuration. By evaluating the composite under both acidic and neutral electrolytes, this study offers a clearer understanding of its stability and energy storage behavior across different operational conditions, thereby improving insight into its overall performance in supercapacitor systems. To the best of our knowledge, this is the first study to systematically investigate the compositional tuning of rGO-MnO_2-PPy nanocomposites and their electrochemical behavior in both acidic and neutral electrolytes under a symmetric cell configuration. The electrode demonstrated effective electrochemical performance in both 0.5 M Na_2SO_4 and 1 M H_2SO_4, highlighting its versatility across different electrolyte environments. Notably, high specific capacitance values were achieved, reaching 475.6 F g^{-1} (20 mV s^{-1}) and 345.87 F g^{-1} (0.5 A g^{-1}) in Na_2SO_4, and 331.76 F g^{-1} and 220.16 F g^{-1} in H_2SO_4. The device also delivered energy densities of 8.65 Wh kg^{-1} and 6.19 Wh kg^{-1} with corresponding power densities of 1421.97 W kg^{-1} and 1512.81 W kg^{-1} in Na_2SO_4 and H_2SO_4, respectively. Furthermore, the electrode exhibited a long cycle life, retaining 88.85% and 86.08% of its initial capacitance after 5000 cycles in Na_2SO_4 and H_2SO_4, respectively. The results indicate that the proposed electrode is a promising candidate

for high-performance supercapacitors capable of operating in multiple electrolyte systems with an extended lifespan.

Experimental Section

Materials

Reduced graphene oxide was supplied from Nanograf Corporation (Turkey). Polypyrrole (≥ 99.5%), sulfuric acid (H_2SO_4) (≥96%), ammonium persulfate (APS), poly(vinylidene fluoride) (PVDF), polyvinylpyrrolidone (PVP, powder, mean Mw 29,000), ammonia (28% w/w), and *N*-methylpyrrolidone (NMP) were purchased from Sigma-Aldrich (Germany). Potassium permanganate ($KMnO_4$) was obtained from Merck (Germany).

Synthesis of MnO_2

For the synthesis of pure MnO_2, 1.9 g of $KMnO_4$ and 400 µL of H_2SO_4 were dissolved in 50 mL of DI water and magnetically stirred for 1 h. Subsequently, the reaction mixture was transferred into a 100 mL Teflon-lined stainless-steel autoclave and subjected to hydrothermal treatment at 140°C for 5 h. The resulting solid was repeatedly purified by washing with deionized water and was finally dried under vacuum at 65°C for 24 h.[46]

Synthesis of rGO-MnO_2 Nanocomposites

The synthesis of rGO-MnO_2 was conducted through a one-step hydrothermal method. Initially, rGO dispersion with a concentration of 1 mg/mL was prepared in deionized water by ultrasonication for 1 h. To investigate the effect of the MnO_2 content on the electrochemical performance, different amounts of $KMnO_4$ ($KMnO_4$:rGO 2:1, 4:1, 6:1 w/w) were added to the prepared rGO dispersion. PVP (5 mg/mL) was added as a stabilizing agent in order to prevent agglomeration.[47,48] Afterward, the mixture was transferred into a Teflon-lined autoclave for hydrothermal processing at 120°C for 12 h. The obtained products were subsequently cleaned through repeated rinsing with deionized water and then dried at 70°C under vacuum conditions.

Synthesis of rGO-MnO_2-PPy Nanocomposites

PPy coating was achieved by *in situ* oxidative polymerization of pyrrole on rGO-MnO_2 nanocomposites. Firstly, a certain amount of rGO-MnO_2 was re-dispersed in 0.1 M H_2SO_4 (30 mL) by ultrasonication. Subsequently, pyrrole was added at different mass ratios (Pyrrole:rGO-MnO_2, m/m, 12:1, 16:1) by sonication, and the mixture was placed in an ice bath and stirred for 1 h. Ammonium persulfate (APS) (APS:pyrrole 1:1 n/n) was added to the mixture to initiate polymerization, and the reaction continued overnight. The synthesized nanocomposites were purified by centrifugation with ethanol and deionized water, followed by drying at 70°C under vacuum conditions. These samples were denoted as follows according to different component ratios: rGO-$MnO_2$2-PPy12 ($KMnO_4$:rGO 2:1, Pyrrole:rGO-MnO_2, m/m, 12:1), rGO-$MnO_2$4-PPy12 ($KMnO_4$:rGO 4:1, Pyrrole:rGO-MnO_2, m/m, 12:1), rGO-$MnO_2$6-PPy12 ($KMnO_4$:rGO 6:1, Pyrrole:rGO-MnO_2, m/m, 12:1), rGO-$MnO_2$2-PPy16 ($KMnO_4$:rGO 2:1, Pyrrole: rGO-MnO_2, m/m, 16:1), rGO-$MnO_2$4-PPy16 ($KMnO_4$:rGO 4:1, Pyrrole:rGO-MnO_2, m/m, 16:1), rGO-$MnO_2$6-PPy16 ($KMnO_4$:rGO 6:1, Pyrrole:rGO-MnO_2, m/m, 16:1).

Characterization

The chemical structures of the samples were characterized by ultraviolet–visible (UV–Vis) spectroscopy (Shimadzu UV-1601, 200–1100 nm) and Fourier transform infrared (FTIR) spectroscopy (Shimadzu 8400-S, 400–4000 cm^{-1}). The crystalline phases were identified using X-ray diffraction (XRD) (Rigaku MiniFlex) with Cu Kα radiation (λ = 0.154 nm) over a 2θ range of 10°–90° at a scan rate of 2 min^{-1}. Morphological features were investigated using field-emission scanning electron microscopy (FESEM; FEI QUANTA 400F) operated at 30 kV and transmission electron microscopy (TEM; JEOL JEM-100CX II). The specific surface area and pore characteristics were obtained using a surface analyzer (Quantachrome AUTOSORB-1C/MS). The surface area of the rGO-MnO_2-PPy nanocomposite was derived from N_2 adsorption/desorption isotherms using the Brunauer–Emmett–Teller (BET) method. The pore size distribution of the samples was evaluated utilizing the Barrett–Joyner–Halenda (BJH) method. The total pore volume was determined from the adsorption data at a relative pressure of 0.99.

Electrode Fabrication and Electrochemical Performance Analysis

Electrochemical measurements of the synthesized nanocomposites were carried out in a two-electrode configuration. The electrode material was drop-coated onto stainless-steel discs with a surface area of 1 cm^2. The electrode material was prepared by mixing electroactive sample (80%), poly(vinylidene fluoride) (PVDF) (8%), and carbon black (12%) in *N*-methyl-2-pyrrolidone (NMP) until a homogeneous slurry was obtained. The electrodes were vacuum-dried at 75°C under vacuum. A Gamry Reference 3000 model potentiostat-galvanostat was used for electrochemical measurements. A Hohsen HS test cell was used as an electrochemical cell in the

two-electrode configuration. Measurements were performed in a scan rate range of 5–200 mV s^{-1} for cyclic voltammetry (CV) analysis, in a frequency range of 0.01–100 kHz for electrochemical impedance spectroscopy (EIS), and in a current density range of 0.5 A g^{-1} to 200 A g^{-1} for galvanostatic charge–discharge (GCD) analysis.

In the two-electrode configuration, the equations used for specific capacitance calculations from CV and GCD analyses are given in Eqs. 1 and 2, respectively.

$$C = \frac{2 \int IdV}{v \times \Delta V \times m}, \tag{1}$$

$$C = \frac{2I \times \Delta t}{\Delta V \times m}, \tag{2}$$

where C (F g^{-1}) denotes the specific capacitance, I (A) represents the applied current, ΔV (V) corresponds to the potential window, V (mV s^{-1}) indicates the scan rate, Δt (s) refers to the discharge duration, and m (g) denotes the mass of the active electrode material.[49]

For the two-electrode system, energy and power densities were evaluated based on Eqs. 3 and 4.

$$E = \frac{1}{2 \times 4 \times 3.6} \times C \times V^2, \tag{3}$$

$$P = \frac{3600 \times E}{\Delta t}. \tag{4}$$

Here, E (Wh kg^{-1}) corresponds to the energy density, while P (W/kg) represents the power density.[49]

Results and Discussion

Chemical Characterization

Figure 1 presents the UV–Vis spectra of MnO_2, rGO, rGO-MnO_2 ($KMnO_4$:rGO 2:1, 4:1, 6:1 w/w) and rGO-MnO_2-PPy16 ($KMnO_4$:rGO 2:1, Pyrrole:rGO-MnO_2, m/m, 16:1) nanocomposites. The absorption band centered around 410 nm originates from intra-d orbital (d–d) transitions associated with Mn cations embedded in the MnO_2 lattice framework.[50] The rGO and rGO-MnO_2 samples exhibit a characteristic peak at 270 nm, corresponding to the π–π* transition of the aromatic C–C bonds in rGO. The incorporation of MnO_2 between the rGO layers leads to a peak shift in the range of 374–460 nm, confirming a robust interaction between rGO and MnO_2. Such interaction alters the electronic structure and reduces the transition energy, thereby inducing a redshift of the absorption peak toward longer wavelengths. In the rGO-$MnO_2$2-PPy16 nanocomposite, the characteristic absorption peak of PPy is observed from

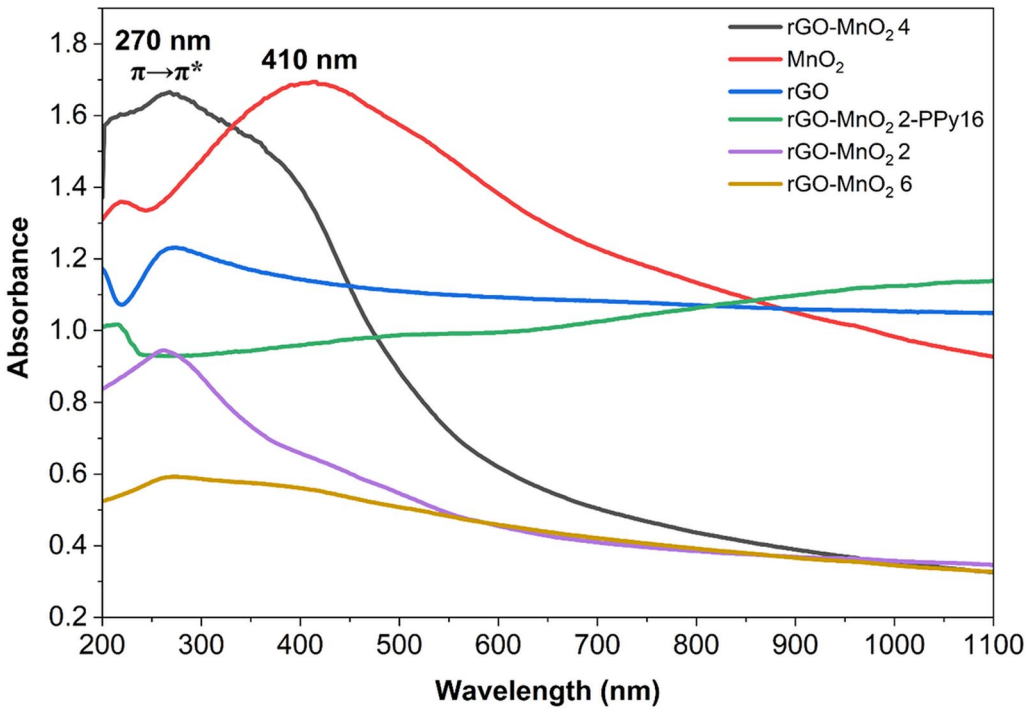
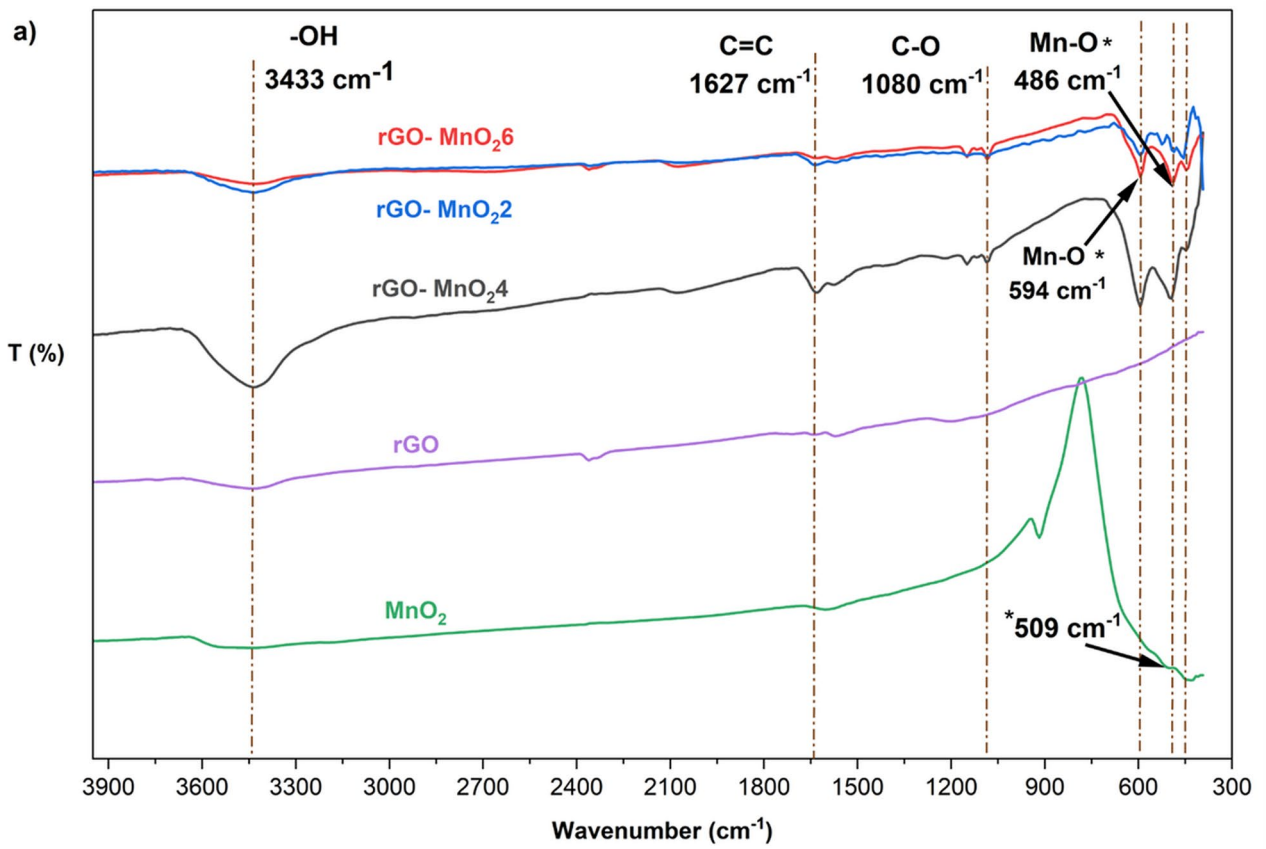
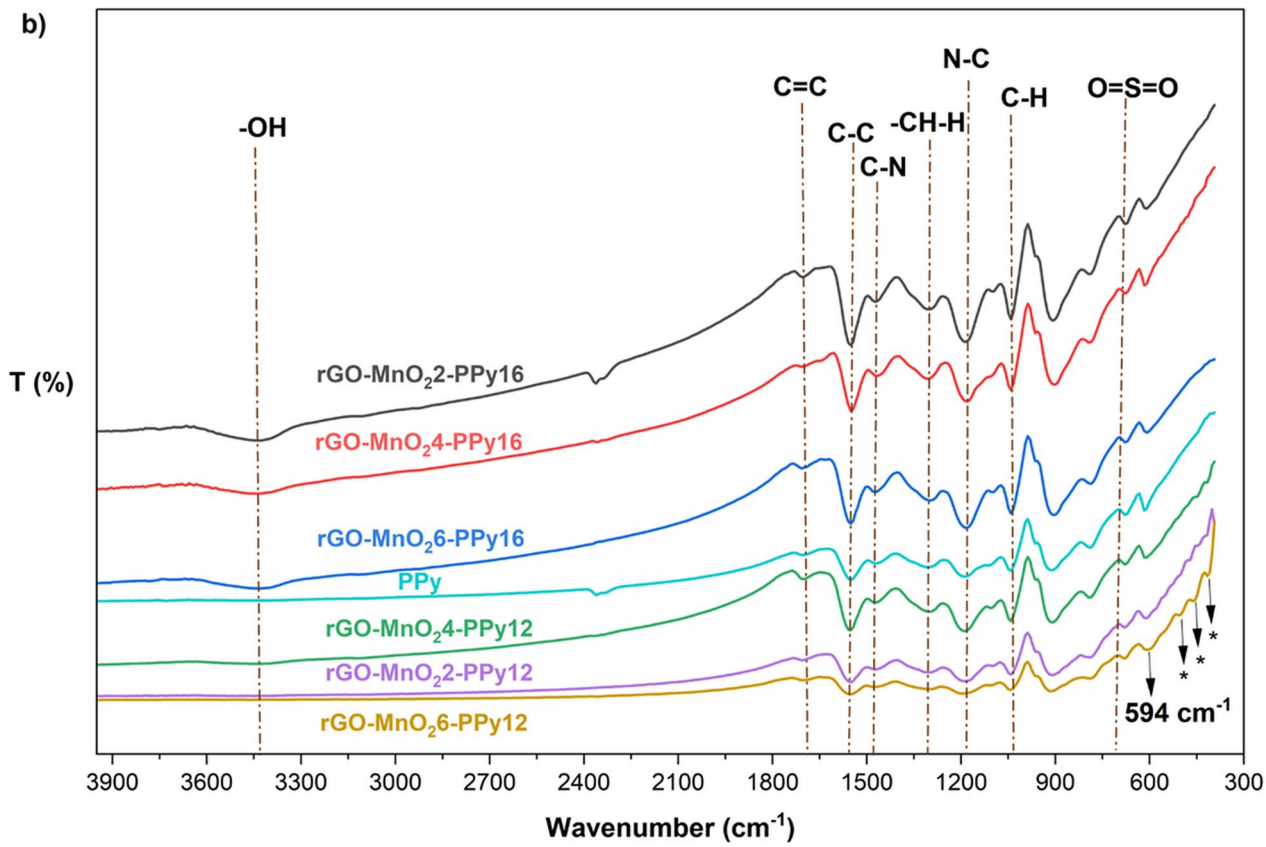


Fig. 1 UV-Vis spectra of the samples of MnO_2, rGO, rGO-MnO_2 ($KMnO_4$:rGO 2:1, 4:1, 6:1 w/w), rGO-$MnO_2$2-PPy16 ($KMnO_4$:rGO 2:1, Pyrrole:rGO-MnO_2, m/m, 16:1).


a)
-OH
3433 cm-1
C=C
1627 cm-1
C-O
1080 cm-1
Mn-O *
486 cm-1
rGO- MnO2 6
rGO- MnO2 2
rGO- MnO2 4
Mn-O *
594 cm-1
T (%)
rGO
MnO2
*509 cm-1
3900 3600 3300 3000 2700 2400 2100 1800 1500 1200 900 600 300
Wavenumber (cm-1)


b)
-OH
C=C
C-C
C-N
-CH-H
N-C
C-H
O=S=O
T (%)
rGO-MnO2 2-PPy16
rGO-MnO2 4-PPy16
rGO-MnO2 6-PPy16
PPy
rGO-MnO2 4-PPy12
rGO-MnO2 2-PPy12
rGO-MnO2 6-PPy12
*
*
*
*
594 cm-1
3900 3600 3300 3000 2700 2400 2100 1800 1500 1200 900 600 300
Wavenumber (cm-1)

◂**Fig. 2** (a) FTIR analysis of pristine MnO_2, rGO and rGO-MnO_2 nanocomposites ($KMnO_4$:rGO 2:1, 4:1, 6:1 w/w) (b) PPy and rGO-MnO_2-PPy ($KMnO_4$:rGO 2:1, 4:1, 6:1 w/w, Pyrrole:rGO-MnO_2, m/m, 12:1, 16:1) nanocomposites.

400 nm to 470 nm and is attributed to the $\pi \rightarrow \pi^*$ electronic transition. However, the absorption features associated with MnO_2 cannot be clearly distinguished in the spectrum due to the coverage of the rGO surface by PPy. In addition, the absorption region between 800 nm and 1000 nm corresponds to electron transitions from the valence band of the conjugated PPy chains to the bipolaron band, reflecting the presence of delocalized polarons along the PPy backbone.[51–55]

Figure 2a shows the FTIR spectra of the pristine MnO_2, pristine rGO, and rGO-MnO_2 nanocomposites. The broad peak appearing at approximately 3433 cm^{-1} in all three nanocomposites is attributed to the –OH stretching vibrations of surface hydroxyl groups. The presence of this band is attributed to residual hydroxyl groups remaining on the rGO structure as a result of incomplete reduction, and it may also correspond to adsorbed water molecules.[52,56] The bands at 1627 cm^{-1} and 1080 cm^{-1} correspond to the C=C stretching vibration of rGO and the C–O stretching of epoxy groups, respectively. In the literature, peaks observed at 563, 509, and 424 cm^{-1} in rod-like pure MnO_2 nanoparticles below 750 cm^{-1} correspond to the characteristic bending vibration of Mn–O bonds.[51,56–58] After incorporation of MnO_2 into the rGO framework, the peaks observed in pure MnO_2 shifted from 563 cm^{-1} to 594 cm^{-1}, from 509 cm^{-1} to 486 cm^{-1}, and from 424 cm^{-1} to 439 cm^{-1}. This indicates strong interfacial interactions between MnO_2 and rGO. These peaks clearly confirm the successful incorporation of MnO_2 into the rGO-MnO_2 nanocomposite framework. Figure 2b displays the FTIR analysis of pristine PPy and rGO-MnO_2-PPy nanocomposites. For pristine PPy, the band at 1543 cm^{-1} arises from the aromatic C–C stretching modes associated with the conjugated pyrrolic backbone. The band observed at 1465 cm^{-1} originates from the C–N skeletal stretching vibrations, reflecting the intrinsic vibrational signatures of the polymer's heteroaromatic framework. The peaks at 1296, 1180, and 1041 cm^{-1} are assigned to the –CH–H vibration, N–C stretching vibration, and C–H deformation vibration, respectively. In both PPy and rGO-MnO_2-PPy nanocomposites, the vibrational feature at approximately 671 cm^{-1} is assigned to the symmetric O=S=O stretching mode, indicative of the presence of H_2SO_4-derived dopant anions within the polymeric matrix.[34,59,60] All characteristic PPy peaks were observed in the rGO-MnO_2-PPy nanocomposites, indicating that PPy was successfully integrated with rGO. In addition, the Mn–O bond vibration bands were most pronounced in the rGO-$MnO_2$6-PPy12 nanocomposite with the highest MnO_2 content due to the surface coating of PPy (594, 501, and 455 cm^{-1}). In the rGO-MnO_2-PPy nanocomposites, the simultaneous presence of characteristic rGO peaks, Mn–O vibrational bands, and PPy-specific signals verifies the successful synthesis and coherent assembly of the hybrid structure.

Figure 3 shows the XRD patterns of rGO, rGO-$MnO_2$2, and rGO-$MnO_2$2-PPy16 nanocomposite. The diffraction pattern of rGO (Fig. 3a) shows a broad peak at 26.32° corresponding to the (002) plane of rGO nanosheets.[51] The rGO-MnO_2 diffraction pattern (Fig. 3b) shows that α-MnO_2 can be indexed according to the tetragonal crystal phase structure (JCPDS no. 44-0141). The diffraction peaks observed at 2θ values are 18.0°, 28.87°, 37.18°, 38.05°, 40.99°, 49.84°, 56.04°, 59.89°, 65.02°, 69.64°, and 73.93° and correspond to the (200), (310), (400), (211), (420), (411), (600), (521), (002), (514), and (312) planes, respectively. There is also a prominent peak of rGO centered around 26.1°. These diffraction peaks confirm that the rGO-$MnO_2$2 composite has been successfully synthesized.[61–64] In the rGO-$MnO_2$2-PPy16 nanocomposite (Fig. 3c), a broad diffraction peak was observed between 20.2° and 26.3°. This peak corresponds to the amorphous structure of PPy.[65] The amorphous PPy layer coated on the surface of MnO_2 nanoparticles during the polymerization process caused the disruption of the crystal structure and consequently the loss of distinctiveness of the characteristic diffraction peaks belonging to MnO_2. As supported by earlier research, this behavior corresponds to the coating of the crystalline MnO_2 phase by an amorphous layer during the PPy polymerization.[66]

Figure 4 shows the BET adsorption–desorption isotherm of rGO-$MnO_2$2-PPy16. The general form of the obtained curve exhibits the character of a type IV isotherm according to IUPAC classification. Type IV isotherms are specific to mesoporous materials and involve monolayer and multilayer adsorption in the low relative pressure region, followed by pore condensation. The distinct separation between the adsorption and desorption branches in the hysteresis loop confirms the mesoporous structure. The BET specific surface area of the nanocomposite was determined to be 116 $m^2\ g^{-1}$. The pore size distribution of the nanocomposite, as can be seen in the inset of Fig. 4, consists of a mixture of micro- and mesopores. While micropores with an average pore size of 18 *Å* contribute to charge-storage capacity by providing a large surface area, mesopores facilitate rapid ion diffusion, thereby accelerating charge–discharge processes. The total pore volume of 0.1345 $cm^3\ g^{-1}$ demonstrates that the material possesses high porosity and a surface structure that is accessible for ion transport. This structure indicates a pore distribution where mesopores dominate ($V_{meso\%}$; 86.62%) despite the limited contribution of micropores ($V_{micro\%}$; 13.38%). Consequently, this dual-pore system offers advantages for supercapacitor applications in terms of high specific capacitance, high rate capability, and excellent cycle stability.[49,67]

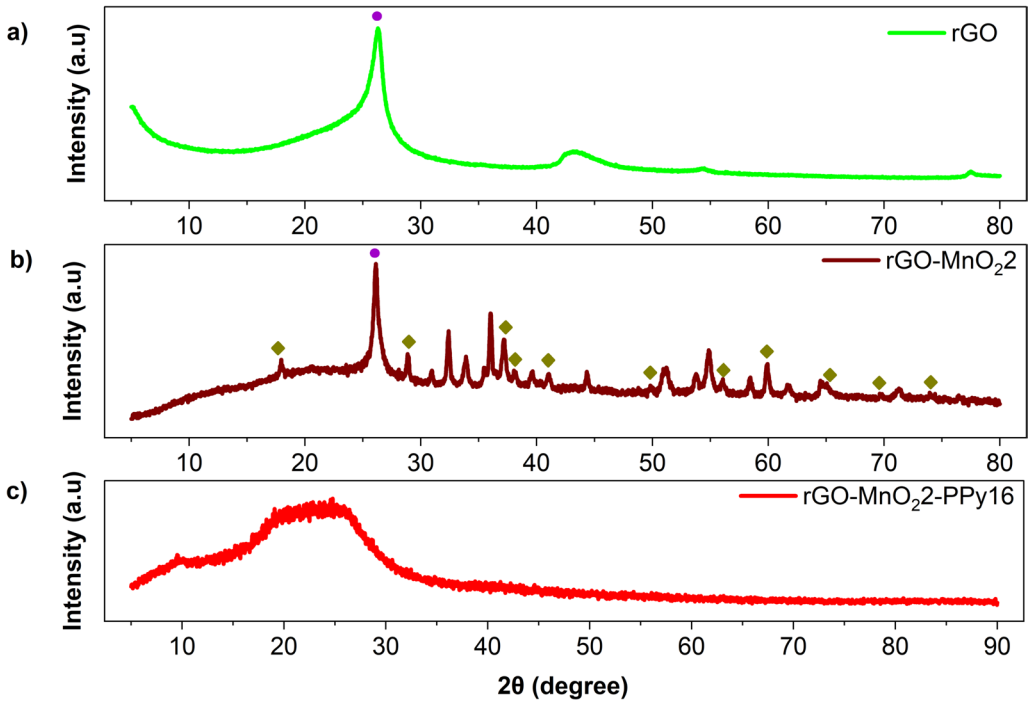


Fig. 3 XRD patterns of (a) rGO, (b) rGO-$MnO_2$2, and (c) rGO-$MnO_2$2-PPy16 nanocomposite.

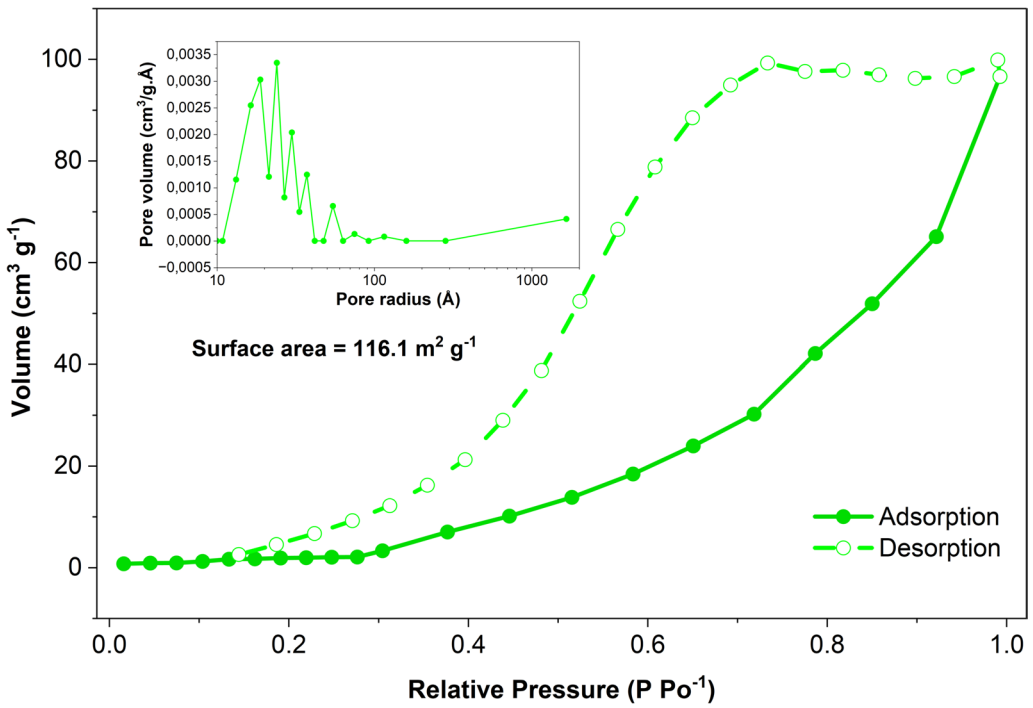


Fig. 4 BET analysis adsorption and desorption isotherms of rGO-$MnO_2$2-PPy16 nanocomposite.

Figure 5 presents the SEM and energy-dispersive X-ray (EDX) analyses of the pristine MnO_2 and rGO-MnO_2 nanocomposite. The SEM images clearly show that MnO_2 is formed in two distinct morphologies: rod-like and layer-like structures (Fig. 5a and b). The EDX spectrum provides additional confirmation of the sample's elemental composition.

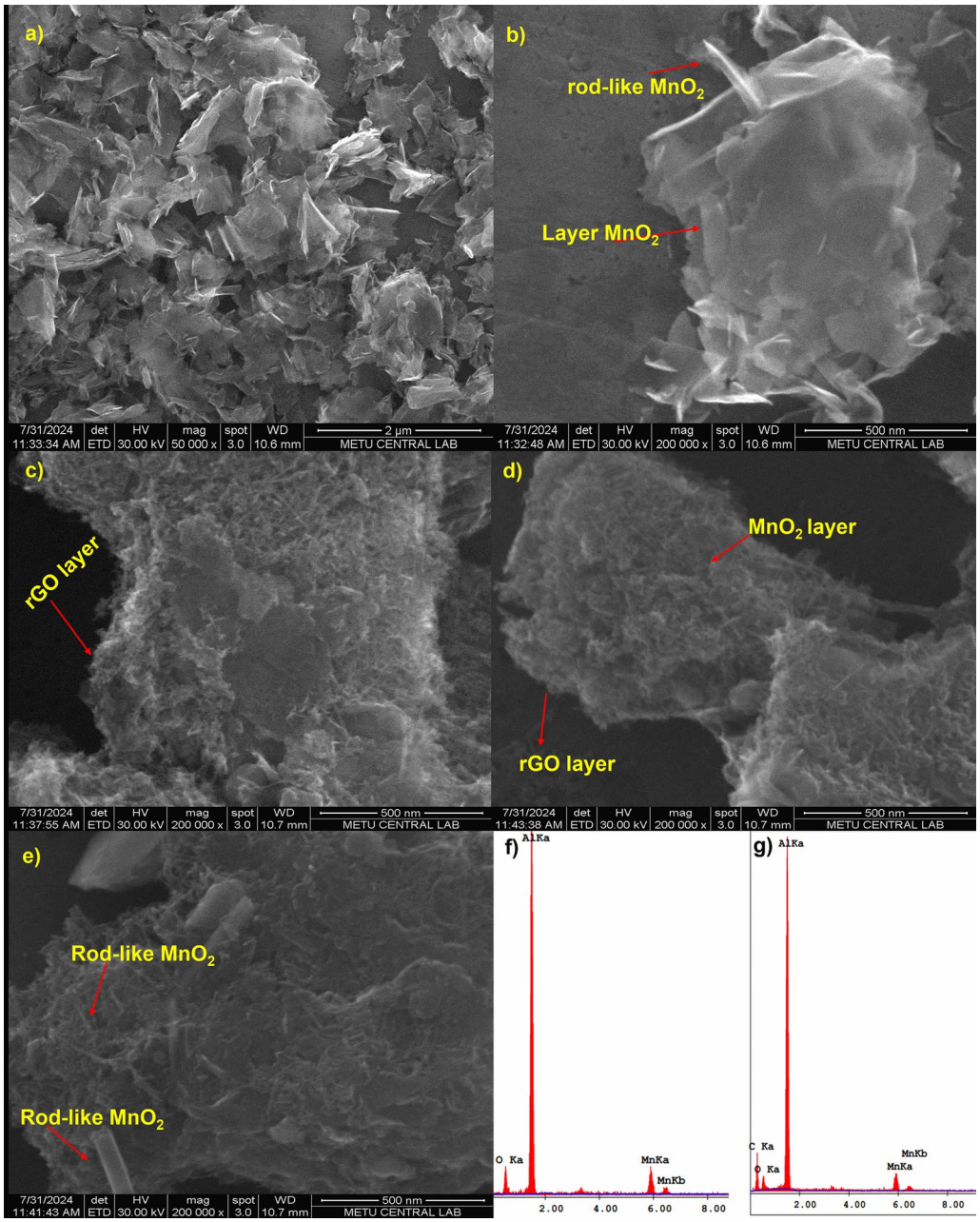


Fig. 5 (a, b) SEM images of pristine MnO_2, (c, d, e) SEM images of rGO-$MnO_2$4 nanocomposite, (f) EDX spectrum of pristine MnO_2, and (g) EDX spectrum of rGO-$MnO_2$4 nanocomposite.

While the Mn signal clearly indicates the presence of MnO_2, the O signal may originate not only from MnO_2 but also from hydroxyl groups present on the surface (Fig. 5f).

In the SEM images (Fig. 5c, d, and e), rod-like and layered MnO_2 nanostructures are densely distributed on the rGO layer. The EDX spectrum (Fig. 5g) further confirms the elemental composition of the nanocomposite: C signals originate exclusively from rGO, O signals from both MnO_2 and rGO, and Mn signals solely from MnO_2. These findings demonstrate the successful formation of MnO_2 on the rGO surface. The proposed formation mechanism of MnO_2 on rGO is provided in Eq. 5. During the reaction, the carbon framework functions as a sacrificial reducing agent that converts MnO_4^- ions in aqueous solution into insoluble MnO_2.[68]

$$4MnO_4^- + 3C + H_2O \text{®} 4MnO_2 + 3CO_3^{-2} + 2HCO_3^- \quad (5)$$

Figure 6a–e present the SEM images of rGO-$MnO_2$2-PPy12, rGO-$MnO_2$2-PPy16, and rGO-$MnO_2$4-PPy16 nanocomposites, and Fig. 6f presents the TEM image of

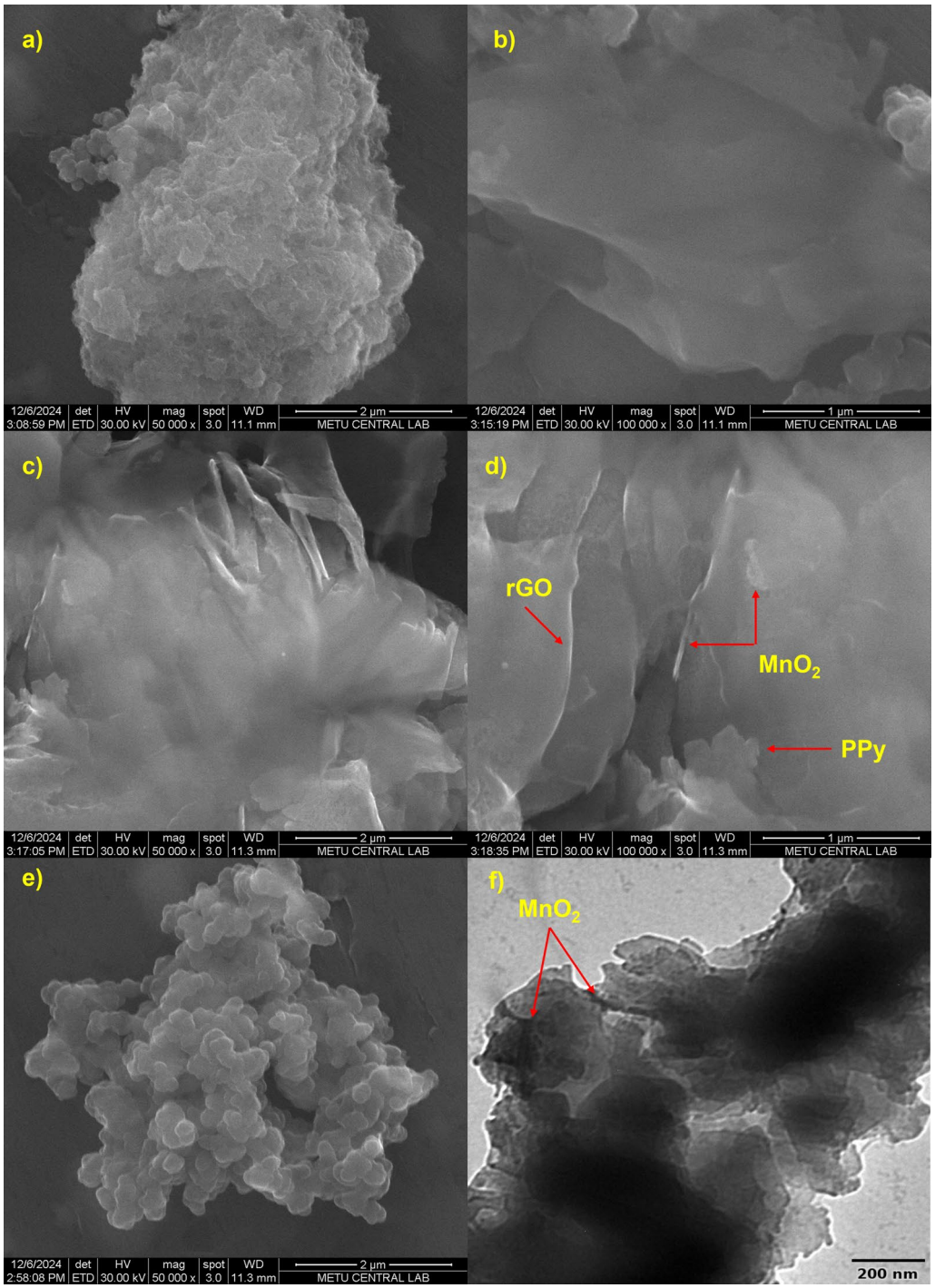


Fig. 6 SEM images of (a, b) rGO-$MnO_2$2-PPy12, (c, d) rGO-$MnO_2$2-PPy16, and (e) rGO-$MnO_2$4-PPy16. (f) TEM image of rGO-$MnO_2$2-PPy16.

rGO-$MnO_2$2-PPy16. Figure 6a and b show that the rGO layer is coated with a PPy layer. In contrast, Fig. 6c and d of the rGO-MnO_2-PPy16 nanocomposite clearly show that the rGO layer is coated with both the PPy polymeric structure and MnO_2. This morphological structure offers significant advantages for supercapacitor applications, including increased surface area, improved electrical conductivity, facilitated ion transport, pseudocapacitive contribution, and enhanced structural stability over long cycles. On the other hand, in the image of the sample obtained by increasing $KMnO_4$ salt and pyrrole monomer together (Fig. 6e), it was determined that the particles tended to form a dense and

granular morphology by aggregation of spherical clusters. Figure 6f shows the TEM image of the rGO-$MnO_2$2–PPy16 nanocomposite, revealing rod-like MnO_2 nanostructures distributed on the surface of the rGO nanosheets. Furthermore, it is evident that the rGO-MnO_2 surface is effectively coated with the PPy polymeric structure.

Electrochemical Characterization

The primary determinants of supercapacitor performance are the intrinsic physicochemical characteristics of the electrode materials and their interfacial interactions with the electrolyte. In addition, the electrode material is expected to exhibit high specific capacitance and enhanced cyclic stability. Firstly, the influence of MnO_2 loading on the electrochemical performance of synthesized rGO-MnO_2 binary nanocomposites was evaluated and compared. The electrochemical measurements of rGO-MnO_2 nanocomposite were conducted in neutral (0.5 M Na_2SO_4) electrolyte in a symmetrical two-electrode configuration between −0.2 V and 0.8 V. The CV curves of pristine rGO, rGO-$MnO_2$2, rGO-$MnO_2$4, and rGO-$MnO_2$6 nanocomposites are shown in Fig. 7a at a scan rate of 20 mV s^{-1}, and CV results for rGO-$MnO_2$6 nanocomposite in the range of 5–100 mV s^{-1} are presented in Fig. 7b. Among the examined samples, rGO-$MnO_2$6 displays the largest enclosed CV area, signifying its superior charge-storage capability relative to pristine rGO, rGO-$MnO_2$2, and rGO-$MnO_2$4 nanocomposites. Specific capacitance values of 40.7, 59.27, 54.98, and 78.33 F g^{-1} were found for rGO and the rGO-$MnO_2$2, rGO-$MnO_2$4, and rGO-$MnO_2$6 nanocomposites, respectively. Additionally, the rGO-$MnO_2$6 composite retained 68.39% of its specific capacitance as the scan rates increased from 5 to 100 mV s^{-1}. In contrast, the rGO-$MnO_2$2 and rGO-$MnO_2$4 nanocomposites exhibited similar specific capacitance values, with retention rates of 80.61% and 77.91%, respectively, which were higher than that of rGO-$MnO_2$6 (Fig. 7c). The higher specific capacitance value of the rGO-$MnO_2$6 nanocomposite relative to the other samples is mainly attributed to the enhanced pseudocapacitive contribution resulting from its

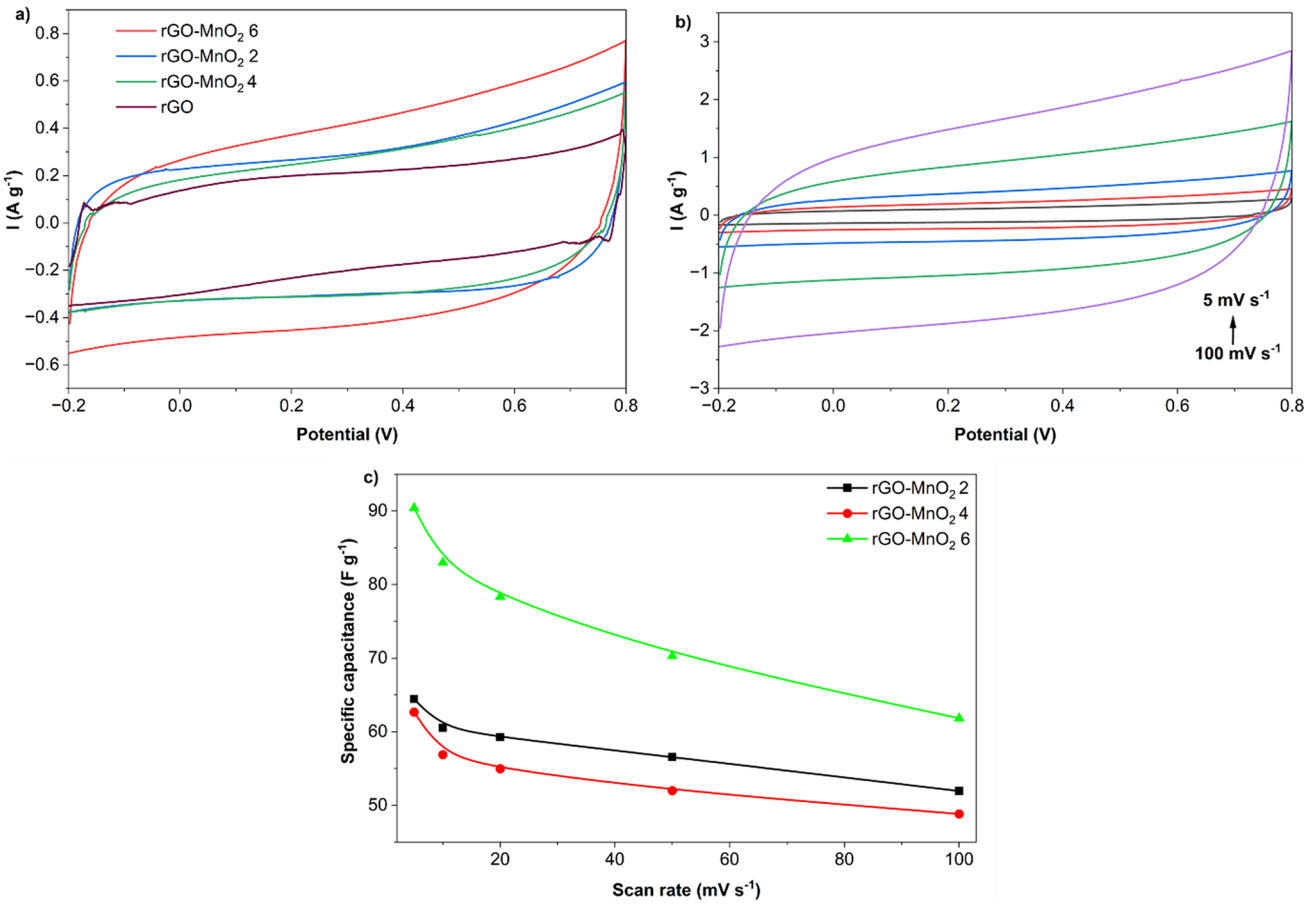


Fig. 7 (a) CV plot comparison of rGO and rGO-MnO_2 nanocomposites at 20 mV s^{-1}. (b) CV analysis of rGO-$MnO_2$6 nanocomposite between 5 and 100 mV s^{-1}. (c) Specific capacitance values obtained from CV analysis of rGO and rGO-MnO_2 binary nanocomposites.

higher MnO_2 content. However, excessive MnO_2 deposition causes agglomeration, decreases conductivity, and increases ion transfer distance and ion diffusion pathways. This may explain the lowest capacitance retention rate observed for rGO-$MnO_2$6 at higher applied scan rates. Also, since MnO_2 is intrinsically less conductive than rGO, the excess amount of MnO_2 may increase the thickness of MnO_2 structures, leading to increased diffusion restrictions, thereby hindering electron transport and ion diffusion. The increased charge transfer resistance and enhanced ion transfer migration distance may cause a decrease in electrochemical performance and deterioration of mechanical integrity.[69,70] Although MnO_2 is well known as a pseudocapacitive material, the CV responses of the binary composites do not exhibit prominent redox peaks, implying that charge storage occurs at a nearly uniform rate during the entire cyclic voltammetry scan.[71,72]

The GCD measurements of binary rGO-MnO_2 nanocomposites are displayed in Fig. 8. rGO-$MnO_2$6 composite exhibited the highest specific capacitance value at current density of 1 A g^{-1}. The specific capacitance values for rGO-$MnO_2$6, rGO-$MnO_2$4, and rGO-$MnO_2$2 were calculated as 43.16, 32.61, and 31.98, respectively. Between 0.5 and 5 A g^{-1}, the capacitance retention value of the rGO-$MnO_2$2 nanocomposite was 71.36%, whereas those of rGO-$MnO_2$6 and rGO-$MnO_2$4 were 61.72% and 66.43%, respectively.

Herein, we report the fabrication of an rGO-MnO_2-PPy hybrid, in which PPy was incorporated into the rGO-MnO_2 structure to enhance the overall electrochemical behavior of the binary nanocomposite. The rGO-MnO_2-PPy nanocomposites were synthesized through the polymerization of PPy on rGO-$MnO_2$6, rGO-$MnO_2$4, and rGO-$MnO_2$2 at different mass ratios (Pyrrole:rGO-MnO_2, m/m, 12:1, 16:1) to investigate the influence of PPy content on capacitive behavior. In this context, rGO-$MnO_2$2-PPy12, rGO-$MnO_2$2-PPy16, rGO-$MnO_2$4-PPy12, rGO-$MnO_2$4-PPy16, rGO-$MnO_2$6-PPy12, and rGO-$MnO_2$6-PPy16 nanocomposites were synthesized. All measurements were conducted in both neutral (0.5 M Na_2SO_4) and acidic (1 M H_2SO_4) electrolytes to evaluate the effect of electrolyte type on the electrochemical performance. Figure 9a shows the CV analysis of rGO-$MnO_2$2-PPy12, rGO-$MnO_2$2-PPy16, rGO-$MnO_2$4-PPy12, rGO-$MnO_2$4-PPy16, rGO-$MnO_2$6-PPy12, and rGO-$MnO_2$6-PPy16 composites in 1 M H_2SO_4, and Fig. 9b shows the CV

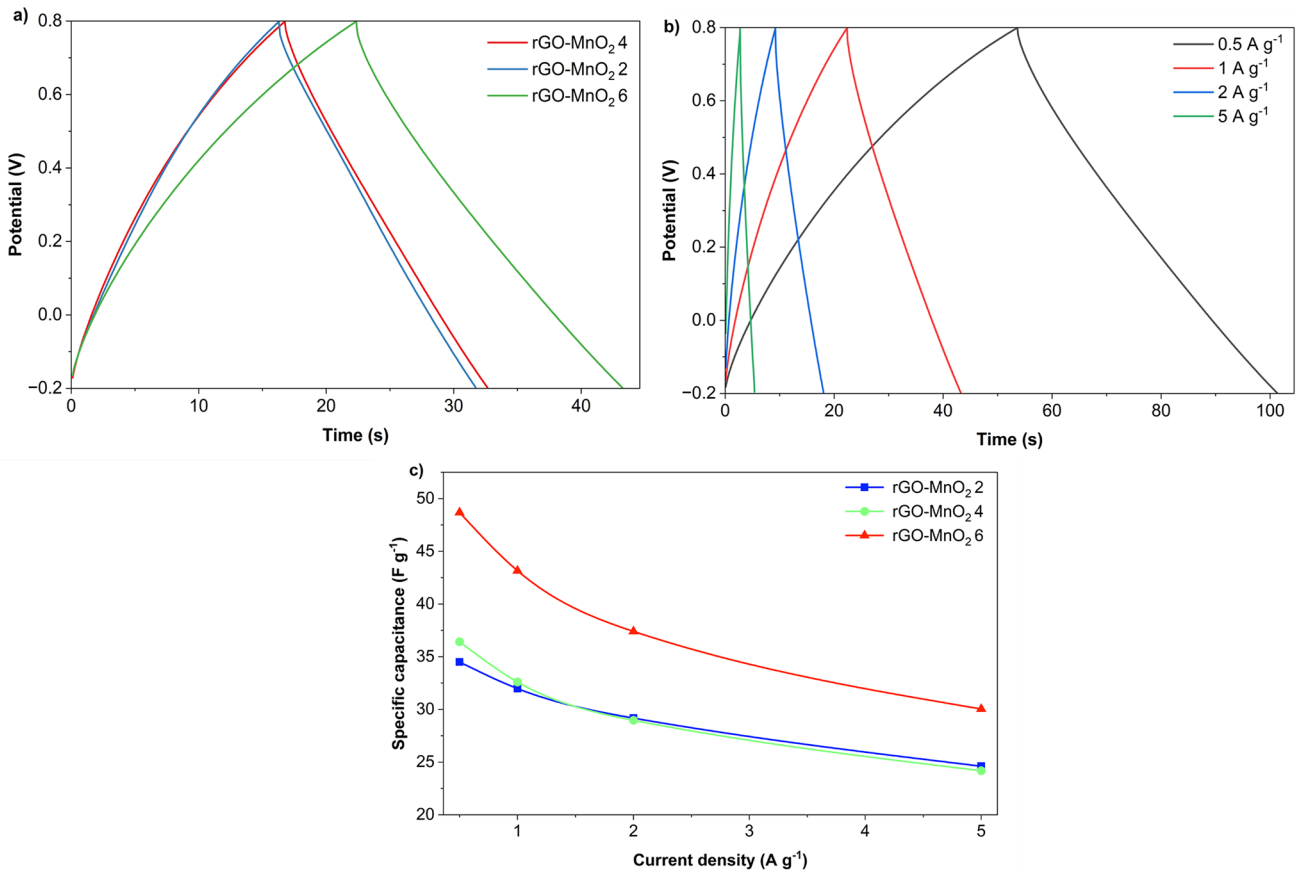


Fig. 8 (a) GCD analysis of binary rGO-MnO_2 nanocomposites at 1 A g^{-1}. (b) GCD analysis of rGO-$MnO_2$6 nanocomposite at 0.5–5 A g^{-1}. (c) Specific capacitance values obtained from GCD analysis of rGO-MnO_2 binary nanocomposites.

curve comparison of ternary nanocomposites at a scan rate of 20 mV s^{-1} in 0.5 M Na_2SO_4. The specific capacitance values of the ternary rGO-MnO_2-PPy nanocomposites obtained by coating the rGO-MnO_2 surface with PPy increased significantly in both H_2SO_4 and Na_2SO_4 electrolytes. Among these electrodes, rGO-$MnO_2$2-PPy16 nanocomposite has the largest enclosed CV area in both H_2SO_4 and Na_2SO_4 electrolytes, indicating superior electrochemical performance and enhanced charge-storage capability in both electrolytes (Tables I and II).

The CV voltammograms of rGO-$MnO_2$2-PPy16 at scan rates ranging from 5 to 100 mV s^{-1} are shown in Fig. 9c for 1 M H_2SO_4 and in Fig. 8d for 0.5 M Na_2SO_4. In 1 M H_2SO_4 at a scan rate of 5 mV s^{-1}, rGO-$MnO_2$2-PPy16 exhibited a specific capacitance of 372.74 F g^{-1} and maintained 65.81% capacitance retention (245.29 F g^{-1}) even at 100 mV s^{-1}. Similarly, a high specific capacitance value of 577.39 F g^{-1} was obtained at 5 mV s^{-1} in 0.5 M Na_2SO_4. At a scan rate of 100 mV s^{-1}, 281.91 F g^{-1} was measured, and 48.82% capacitance retention was achieved between 5 and 100 mV s^{-1}.

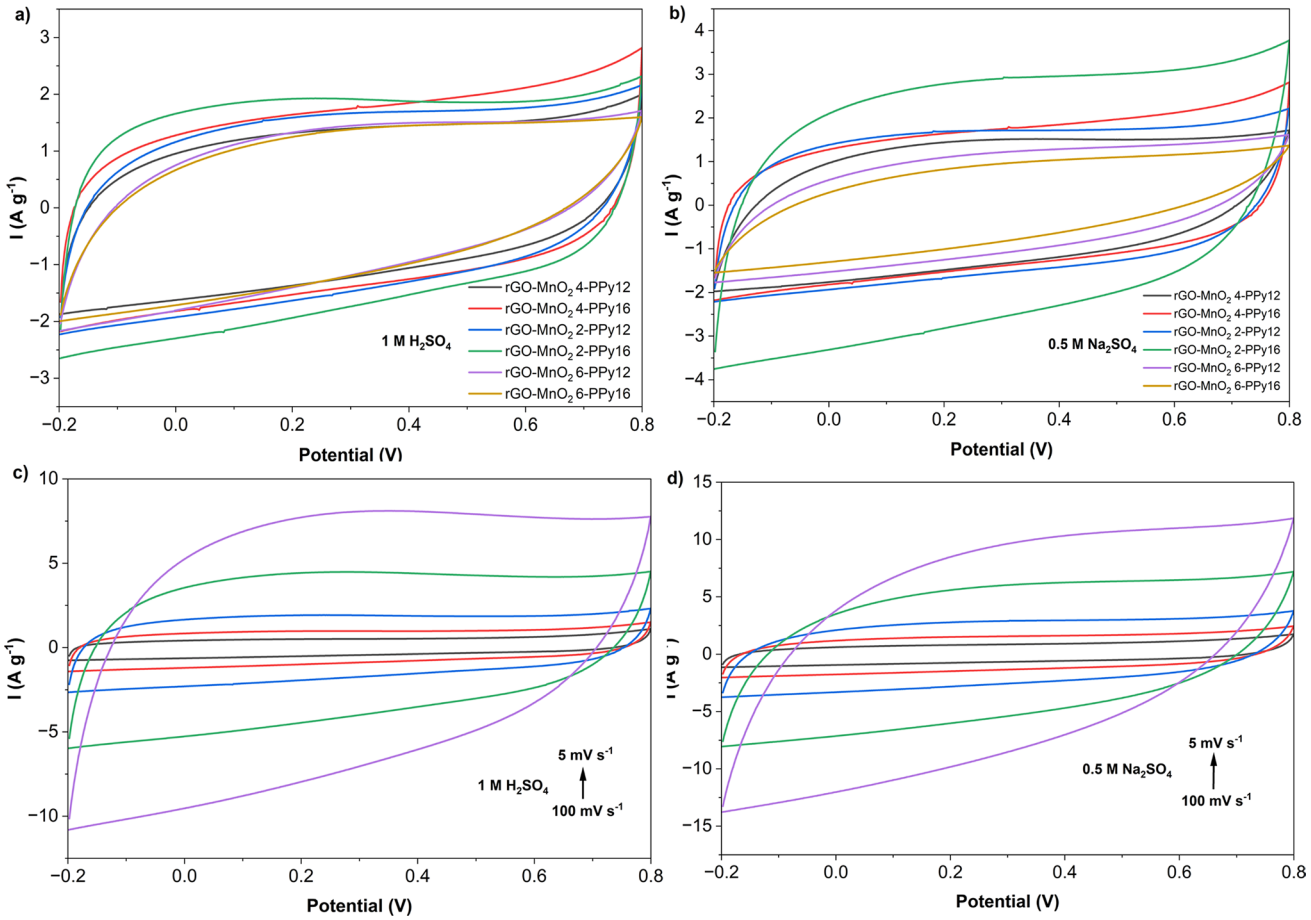


Fig. 9 (a) CV analysis of ternary nanocomposites at 20 mV s^{-1} in 1 M H_2SO_4. (b) CV analysis of ternary nanocomposites at 20 mV s^{-1} in 0.5 M Na_2SO_4. (c) CV analysis of rGO-$MnO_2$2-PPy16 between 5 and 100 mV s^{-1} in 1 M H_2SO_4. (d) CV analysis of rGO-$MnO_2$2-PPy16 between 5 and 100 mV s^{-1} in 0.5 M Na_2SO_4.

Table I Specific capacitance values (in F g^{-1}) of rGO-MnO_2-PPy nanocomposites obtained from CV analysis in 1 M H_2SO_4

Electrode	5 mV s^{-1}	10 mV s^{-1}	20 mV s^{-1}	50 mV s^{-1}	100 mV s^{-1}	Retention (5–100 mV s^{-1})
rGO-$MnO_2$2-PPy12	325.11	300.80	272.61	220.31	172.48	53.05%
rGO-$MnO_2$2-PPy16	**372.74**	**350.32**	**331.76**	**291.18**	**245.29**	**65.81%**
rGO-$MnO_2$4-PPy12	282.45	255.59	228.20	180.13	139.96	49.55%
rGO-$MnO_2$4-PPy16	231.00	223.76	223.23	211.81	195.45	84.61%
rGO-$MnO_2$6-PPy12	318.78	266.61	213.20	140.92	91.72	28.77%
rGO-$MnO_2$6-PPy16	304.41	256.76	204.61	130.65	81.26	26.69%

Bold values indicate the selected composite exhibiting the best electrochemical performance

Among the ternary composites, rGO-$MnO_2$4-PPy16 nanocomposite stands out by exhibiting high rate capability in both electrolytes. To gain further insight into the charge–discharge behavior and rate-dependent stability, GCD measurements were conducted for the ternary nanocomposites.

Figure 10a and b illustrate the GCD curves of the rGO-MnO_2-PPy nanocomposites measured at a current density of 1 A g^{-1} in 1 M H_2SO_4 and 0.5 M Na_2SO_4, respectively. Tables III and IV present electrochemical properties derived from the GCD measurements. Based on these results, the rGO-$MnO_2$2-PPy16 sample demonstrated the most favorable electrochemical behavior, as evidenced by its longer discharge time. The rGO-$MnO_2$2-PPy16 electrode delivered a specific capacitance of 220.16 F g^{-1} in 1 M H_2SO_4, retaining 70.51% of its capacitance (155.24 F g^{-1}) at 20 A g^{-1}, signifying strong rate capability. In 0.5 M Na_2SO_4, this electrode reached 345.87 F g^{-1} at 0.5 A g^{-1} and 249.13 F g^{-1} at 20 A g^{-1}, while the capacitance retention over the current density range of 0.5–20 A g^{-1} was calculated as 72.03%. rGO-$MnO_2$4-PPy16 nanocomposite also showed

Table II Specific capacitance values (in F g^{-1}) rGO-MnO_2-PPy nanocomposites obtained from CV analysis in 0.5 M Na_2SO_4

Electrode	5 mV s^{-1}	10 mV s^{-1}	20 mV s^{-1}	50 mV s^{-1}	100 mV s^{-1}	Retention (5–100 mV s^{-1})
rGO-$MnO_2$2-PPy12	341.50	316.25	290.50	237.95	186.70	54.67%
rGO-$MnO_2$2-PPy16	**577.39**	**529.13**	**475.65**	**372.98**	**281.91**	**48.82%**
rGO-$MnO_2$4-PPy12	311.11	275.99	233.72	160.76	103.86	33.38%
rGO-$MnO_2$4-PPy16	299.16	294.37	292.97	271.25	244.59	81.76%
rGO-$MnO_2$6-PPy12	280.24	236.26	185.75	116.21	72.33	25.81%
rGO-$MnO_2$6-PPy16	236.12	190.71	137.27	71.88	39.14	16.58%

Bold values indicate the selected composite exhibiting the best electrochemical performance

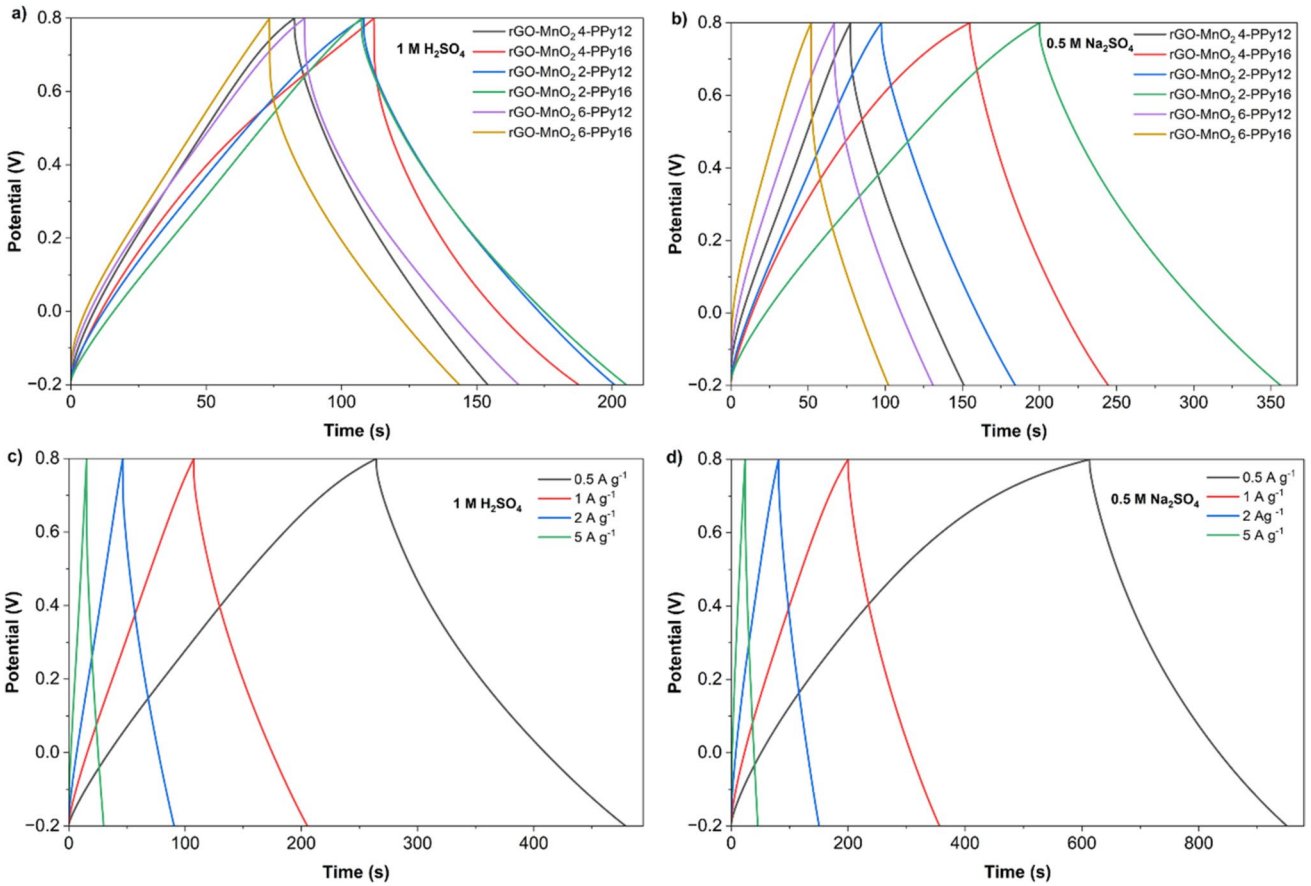


Fig. 10 (a) GCD analysis of ternary nanocomposites at 1 A g^{-1} in 1 M H_2SO_4. (b) GCD analysis of ternary nanocomposites at 1 A g^{-1} in 0.5 M Na_2SO_4. (c) GCD analysis of rGO-$MnO_2$2-PPy16 between 0.5 and 5 A g^{-1} in 1 M H_2SO_4. (d) GCD analysis of rGO-$MnO_2$2-PPy16 between 0.5 and 5 A g^{-1} in 0.5 M Na_2SO_4.

Table III Specific capacitance values (in F g^{-1}) obtained from GCD analysis of rGO-MnO_2-PPy nanocomposites in 1 M H_2SO_4

Electrode	0.5 A g^{-1}	1 A g^{-1}	2 A g^{-1}	5 A g^{-1}	10 A g^{-1}	20 A g^{-1}	Retention (0.5–5 A g^{-1})
rGO-$MnO_2$2-PPy12	203.64	193.41	176.9	150.68	127.39	101.27	73.99%
rGO-$MnO_2$2-PPy16	**220.16**	**204.35**	**191.61**	**178.39**	**170.16**	**155.24**	**81.03%**
rGO-$MnO_2$4-PPy12	163.16	148.82	132.89	107.58	87.39	66.04	65.94%
rGO-$MnO_2$4-PPy16	215	168.21	152.14	138.21	128.69	118.82	64.28%
rGO-$MnO_2$6-PPy12	190	170.14	140.81	100.08	64.68	18.58	52.67%
rGO-$MnO_2$6-PPy16	183.63	159.12	132.25	87.07	42.27	–	47.42%

Bold values indicate the selected composite exhibiting the best electrochemical performance

Table IV Specific capacitance values (in F g^{-1}) obtained from GCD analysis of rGO-MnO_2-PPy nanocomposites in 0.5 M Na_2SO_4

Electrode	0.5 A g^{-1}	1 A g^{-1}	2 A g^{-1}	5 A g^{-1}	10 A g^{-1}	20 A g^{-1}	Retention (0.5-5 A g^{-1})
rGO-$MnO_2$2-PPy12	189.75	180	163.5	132.13	108.88	86.55	69.63%
rGO-$MnO_2$2-PPy16	**345.87**	**323.91**	**292.17**	**249.13**	**212.33**	**177.04**	**72.03%**
rGO-$MnO_2$4-PPy12	173.33	159.72	140.69	105.58	71.51	–	60.91%
rGO-$MnO_2$4-PPy16	208.82	183.03	175.79	161.97	148.95	132.13	77.56%
rGO-$MnO_2$6-PPy12	166.25	142.50	114.4	73.32	37.31	–	44.10%
rGO-$MnO_2$6-PPy16	146.63	121.63	88.84	36.29	–	–	24.75%

Bold values indicate the selected composite exhibiting the best electrochemical performance

remarkable electrochemical performance, exhibiting capacitance of 208.82 F g^{-1} at 0.5 A g^{-1} in 0.5 M Na_2SO_4 and capacitance retention of 77.56% up to 5 A g^{-1}. As a result, the rGO-$MnO_2$2-PPy16 nanocomposite achieved higher specific capacitance values compared to rGO-$MnO_2$4-PPy16 in both 1 M H_2SO_4 and 0.5 M Na_2SO_4. The PPy coating increased the pseudocapacitive charge storage on the rGO-MnO_2 surface and compensated the low intrinsic conductivity of MnO_2, thus enabling more charge-storage capability. This may have contributed to the increase in specific capacitance. Furthermore, the conductive PPy matrix decreases ion transfer migration length and facilitates faster access of electrolyte ions to the active sites. The PPy coating aids in preserving the MnO_2 nanostructures embedded in the polymer network and supports their charge-storage behavior through the pseudocapacitive mechanism. In addition, the MnO_2 and rGO nanosheets reinforce the polymer framework, enabling the electrode to retain its structural integrity and stability throughout the charge–discharge cycles. The enhanced electrochemical behavior of the rGO-MnO_2-PPy electrodes reflects their increased specific capacitance, reduced internal resistance, and efficient ion-transport kinetics. The electrolyte structure has a significant impact on charge transfer resistance; as reported in the literature, this is expressed as an increase in H_2SO_4, NaCl, and KOH electrolytes in the order of 1 M H_2SO_4 < 1 M NaCl < 1 M KOH. When comparing Na_2SO_4 and H_2SO_4, the hydrated ionic radius of H^+ ions (2.80 Å) in H_2SO_4 is smaller than that of Na^+ (3.58 Å) in Na_2SO_4. This allows H^+ ions to access the inner surface of electrode materials more easily and quickly compared to Na^+ ions, leading to lower resistance and faster ion dynamics.[73,74]

EIS was utilized to characterize the resistive and interfacial properties of the nanocomposites. In the Nyquist diagram, the semicircle appearing in the high-frequency region corresponds to the charge transfer resistance (R_{ct}) at the electrode–electrolyte interface, whereas the low-frequency region is indicative of the capacitive behavior typical of supercapacitor electrodes. Additionally, parameters such as the ionic resistance of the electrolyte, the interfacial contact resistance between the active material and the current collector, and the equivalent series resistance (R_s) of the electrodes can be determined from the point where the impedance semicircle intersects the real axis. The Warburg impedance, appearing as a diffusion-controlled feature,

reflects ion-transport limitations within the electrode matrix, a factor that significantly governs the overall electrochemical performance. It is typically represented as a 45° line on a Nyquist plot at low frequencies. A smaller Warburg impedance reflects reduced diffusion-controlled impedance at the electrode–electrolyte interface, suggesting enhanced ion-transport kinetics. The Warburg coefficient (σ) describes diffusion-controlled processes in an electrochemical system. It expresses the relationship between impedance and the frequency of the applied signal, particularly illustrating the effect of mass transport on the electrochemical reaction.[75–78]

Table V shows the R_s, R_{ct}, and σ values of the nanocomposites in two electrolytes. These values were obtained using the equivalent circuit model shown in Fig. 11. According to the Nyquist plots (Fig. 11) and the data summarized in Table V, the rGO-$MnO_2$4-PPy16 electrode exhibited the lowest R_{ct} and displayed the most favorable overall impedance behavior in both electrolytes, with R_{ct} values of 0.85 Ω in H_2SO_4 and 1.51 Ω in Na_2SO_4. Overall, the H_2SO_4 electrolyte yielded lower resistance values than Na_2SO_4, and the rGO-$MnO_2$2-PPy16 and rGO-$MnO_2$4-PPy16 nanocomposites emerged as the most promising candidates for efficient interfacial charge transfer and rapid ion transport. In addition to the EIS analysis, the CV and GCD analyses confirmed that the highest specific capacitance was achieved with the rGO-$MnO_2$2-PPy16 electrodes. As seen in the SEM

Table V EIS analysis results of rGO-MnO_2-PPy nanocomposites in acidic and neutral electrolyte

Electrode	Electrolyte					
	1 M H_2SO_4			0.5 M Na_2SO_4		
	R_s (Ω)	R_{ct} (Ω)	σ (Ω·s$^{1/2}$)	R_s (Ω)	R_{ct} (Ω)	σ (Ω·s$^{1/2}$)
rGO-$MnO_2$2-PPy12	0.84	3.25	7.87	1.23	3.48	7.41
rGO-$MnO_2$2-PPy16	0.52	2.84	6.49	1.01	6.16	8.30
rGO-$MnO_2$4-PPy12	0.68	4.81	13.17	1.06	12.11	16.39
rGO-$MnO_2$4-PPy16	0.65	0.85	3.65	0.91	1.51	3.45
rGO-$MnO_2$6-PPy12	0.82	10.02	21.61	1.22	18.45	22.83
rGO-$MnO_2$6-PPy16	0.54	8.76	17.15	1.10	28.90	30.25

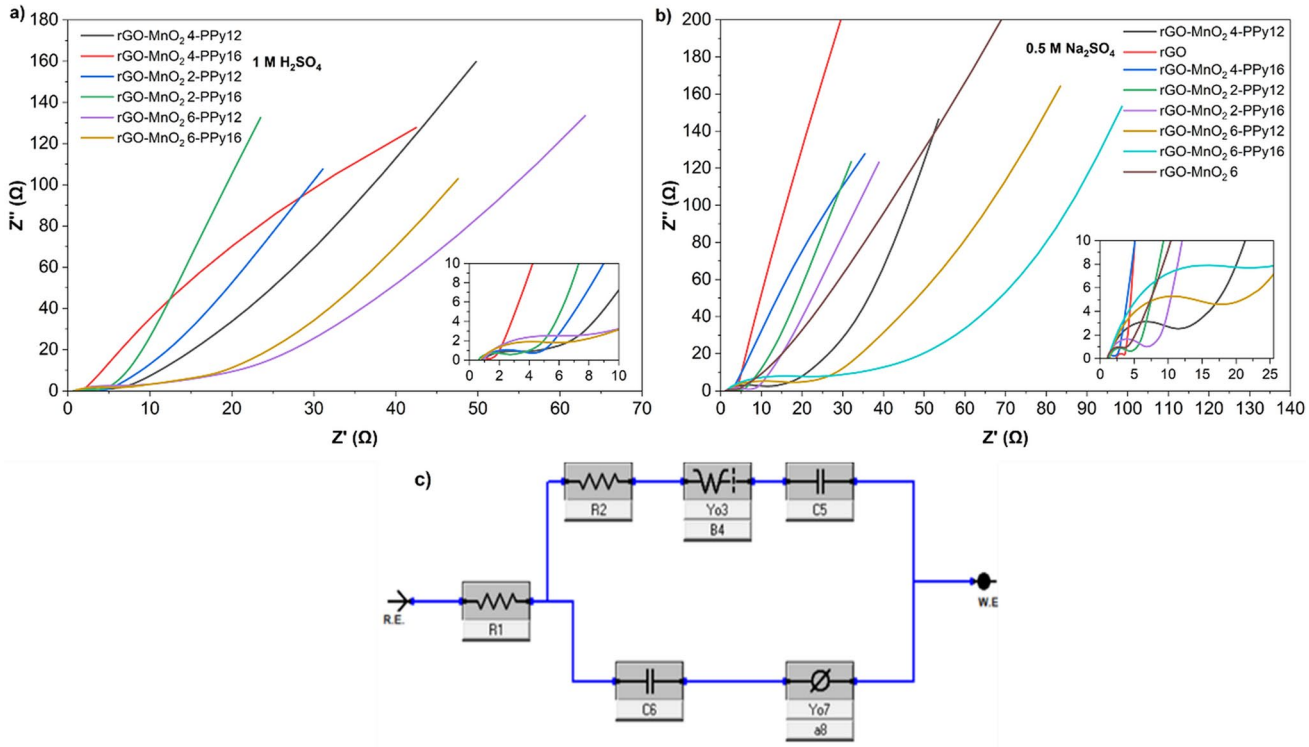


Fig. 11 (a) Nyquist plots of rGO-MnO_2-PPy nanocomposites in 1 M H_2SO_4. (b) Nyquist plots of rGO, MnO_2, and rGO-MnO_2-PPy nanocomposites in 0.5 M Na_2SO_4. (c) Equivalent series circuit used to calculate R_s and R_{ct} values.

images (Fig. 6d and e), both nanocomposites contain the same amount of PPy; however, variations in the rGO-MnO_2 ratio led to different surface morphologies. Although the rGO-$MnO_2$4-PPy16 nanocomposite exhibits lower resistance values, its specific capacitance remains lower than that of rGO-$MnO_2$2-PPy16. This is ascribed to the lower $KMnO_4$ loading in rGO-$MnO_2$2-PPy16, which provides a more favorable balance between electronic conductivity (through the rGO/PPy network) and the redox contribution of MnO_2, thereby enabling more effective surface utilization and improved ion diffusion.

To evaluate the long-term stability of the rGO-$MnO_2$2-PPy16 nanocomposite in both electrolytes, cycling tests were performed for 5000 charge–discharge cycles at a current density of 10 A g^{-1}. Figure 12a illustrates the variation of specific capacitance of rGO-$MnO_2$2-PPy16 as a function of cycle number in 0.5 M Na_2SO_4 electrolyte. In addition, CV analysis (Fig. 12b) performed on rGO-$MnO_2$2-PPy16 electrodes after 5000 cycles in 0.5 M Na_2SO_4 electrolyte yielded post-cycle specific capacitance values of 533.28, 486.07, 427.15, 332.26, 259.47 F g^{-1} at scan rates of 5, 10, 20, 50, and 100 mV s^{-1}, respectively. Moreover, the GCD analysis (Fig. 12c) of post-cycle electrodes exhibited specific capacitance values of 302.17, 288.48, 266.96, 220.87, 187.43, 154.11 F g^{-1} for 0.5, 1, 2, 5, 10, and 20 A g^{-1}, respectively. The CV analysis of rGO-$MnO_2$2-PPy16 nanocomposite after 5000 cycles retained a nearly rectangular shape, indicating good electrochemical reversibility, although a slight shrinkage was observed due to capacitance loss. Similarly, the GCD profiles maintained a symmetric charge–discharge pattern, confirming good reversibility, while the shorter discharge time reflects a decrease in capacitance. After 5000 charge–discharge cycles in 0.5 M Na_2SO_4, rGO-$MnO_2$2-PPy16 retained 88.85% of its specific capacitance, demonstrating excellent electrochemical stability. The results obtained after 5000 charge–discharge cycles clearly demonstrate that the rGO-$MnO_2$2-PPy16 electrode maintains its structural stability in Na_2SO_4 electrolyte. The TEM image of the rGO-$MnO_2$2-PPy16 electrode material obtained after 5000 charge–discharge cycles is presented in Figure 1S. The image clearly demonstrates that the MnO_2 and PPy particles remain firmly anchored on the rGO layers without any significant structural degradation, indicating that the composite exhibits excellent structural stability even after extended cycles. Post-cycle EIS analysis (Fig. 12d) revealed that the R_s and R_{ct} values were 1 and 4.72 Ω, respectively, in Na_2SO_4 electrolyte. The relative decrease in R_s and R_{ct} values after 5000 cycles may be attributed to better electrode–electrolyte contact, a more uniform conductive network formed during cycling, and increased participation of internal pores, which enhances the active surface area during electrochemical operation. This allows electrons and ions to move more easily, resulting in lower R_s and R_{ct} values; moreover, the electrochemical and mechanical stability of the material may also contribute to this behavior.[79,80] Therefore, both the low specific capacitance loss and the decrease in resistance indicate the ability of the material to maintain its performance at high cycle stability. In contrast, it exhibited a remarkable 86.08% capacitance retention after 5000 charge–discharge cycles in H_2SO_4 electrolyte (Figure 2Sa), but the increase in R_{ct} observed after cycling (Figure 2Sb) can probably be attributed to the gradual electrochemical degradation of the composite, especially the over-oxidation of the PPy phase and the difficulty of charge transfer processes due to the degradation of the electrode–electrolyte interface under acidic conditions.[81] At 5 A g^{-1}, the cell exhibited an energy density of 8.65 Wh kg^{-1} and a power density of 1421.97 W kg^{-1} in 0.5 M Na_2SO_4, while in 1 M H_2SO_4 it showed 6.19 Wh kg^{-1} and 1512.81 W kg^{-1}, respectively. Based on electrode capacitance, the energy densities were 34.6 Wh kg^{-1} in Na_2SO_4 and 24.76 Wh kg^{-1} in H_2SO_4. The corresponding Ragone plot is presented in Fig. 12e. When compared to similar electrodes reported in the literature, the rGO-$MnO_2$2-PPy16 electrode has been able to significantly maintain its specific capacitance and energy-power performance in both neutral and acidic electrolytes, even at high current densities. This result is consistent with the electrode's superior rate capability and overall electrochemical efficiency.[82–90]

The rGO-MnO_2-PPy nanocomposite combines the charge-storage capability of PPy with the mechanical strength and electrical conductivity of rGO, while the pseudocapacitive contribution of MnO_2 creates a synergistic effect. When properly dispersed, MnO_2 nanostructures generate more active sites on the electrode surface, facilitating easier access of electrolyte ions and faster charge transfer. In this hybrid system, rGO provides robust mechanical support, PPy ensures conductivity, and MnO_2 contributes redox capacitance, thereby enhancing both stability and overall electrochemical performance.[91–97]

Table VI summarizes previously reported graphene, metal oxide, conductive polymer-based nanocomposites for supercapacitor applications. Unlike most of the studies presented in the table, this work was carried out using a two-electrode configuration. Compared with the three-electrode configuration, which can yield comparatively exaggerated electrochemical performance values, the two-electrode configuration, which is representative of a commercial supercapacitor architecture, provides more realistic electrochemical results for practical supercapacitor applications. Comparative analysis reveals that high specific capacitance values were obtained with rGO-$MnO_2$2-PPy16 nanocomposite in both 1 M H_2SO_4 and 0.5 M Na_2SO_4 electrolytes. In particular, the specific capacitance values of 475.6 F g^{-1} (at 20 mV s^{-1}) and 345.87 F g^{-1} (at 0.5 A g^{-1}) in 0.5 M Na_2SO_4 electrolyte are comparatively higher than many reported studies and indicate the excellent energy storage capacity

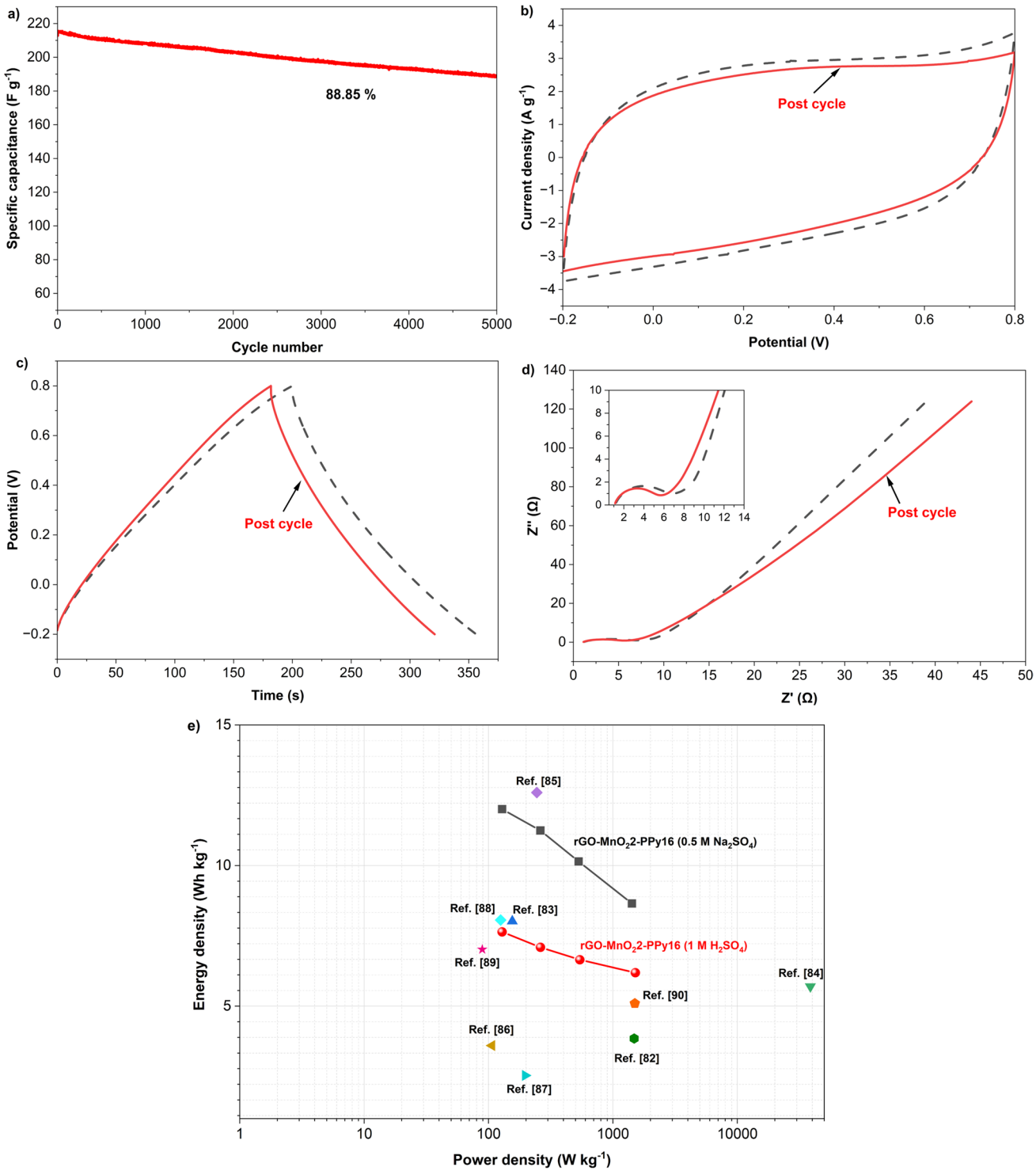


Fig. 12 (a) Capacitance retention of rGO-$MnO_2$2-PPy16 nanocomposite in 0.5 M Na_2SO_4 electrolyte at 10 A g^{-1} current density for 5000 cycles. (b) CV curve of rGO-$MnO_2$2-PPy16 nanocomposite post cycling in 0.5 M Na_2SO_4 electrolyte 20 mV s^{-1}. (c) GCD curve at 1 A g^{-1}. (d) Nyquist curve shift in 0.5 M Na_2SO_4. (e) Ragone plot for rGO-$MnO_2$2-PPy16 and studies in the literature.

of the nanocomposite. The nanocomposite showed effective performance in both acidic (1 M H_2SO_4) and neutral (0.5 M Na_2SO_4) electrolytes. This demonstrates the capacity of the nanocomposite to adapt to different operating environments, which can provide versatility for practical supercapacitor applications. Overall, these findings demonstrate that the

Table VI Supercapacitor applications of nanocomposites based on graphene, metal oxide, conductive polymer

Electrode material	Conf.	Electrolyte	Specific capacitance (F g^{-1})	Rate capability (F g^{-1})	Cyclic stability (%)	Energy density (Wh kg^{-1})	Pover density (W kg^{-1})	Refs.
PPy/GO/ZnO	2E	1 M Na_2SO_4	94.6 (1 A g^{-1})	…	74 % (1000 cycles)	10.65	258.26	82
PPy/ZnO	3E	1 M KCl	161.02 (0.5 A g^{-1})	…	70.71% (5000 cycles)	8.02	155	83
RGO–PPy	3E	3 M KCl	224 (240 A g^{-1})	-	83 % (5000 cycles)	2.5	38600	84
PPy/MGO	2E	2 M $NaNO_3$	202 F g^{-1}	…	83.8 % (1000 cycles)	10	87	85
PPy-NTs/AuNPs	2E	1 M H_2SO_4 PVA	…	…	88 % (2000 cycles)	3.6	106.45	86
rGO/PPy/CB	2E	1 M H_2SO_4	48 F g^{-1}	…	99.9 % (1000 cycles)	2.537	196.2	87
rGO-pg-CN/PPyNTs	3E	1 M KCl	232.21 F g^{-1} (0.5 A g^{-1})	71.52 F g^{-1} (4 A g^{-1})	82% (5000 cycles)	8.063	125	88
PPy–graphene	2E	3 M KCl	255.7 F g^{-1} (0.2 A g^{-1})	199.6 F g^{-1} (25.6 A g^{-1})	93% (1000 cycles)	7.02	89	89
PPy@Nanocellulose@GO	3E	2 M NaCl	244 F g^{-1} (0.2 A g^{-1})	90 F g^{-1} (10 A g^{-1})	85 % (16000 cycles)	5.1	1500	90
PPy/rGO/Fe_2O_3	3E	1 M KCl	125.7 (0.5 A g^{-1})	…	81.3% (200 cycles)	…	…	98
MnO_2/PPy/rGO	3E	1 M Na_2SO_4	404 (0.25 A g^{-1})	120 (4 A g^{-1})	91% (5000 cycles)	-	-	37
PPy/$MnFe_2O_4$/rGO	3E	1 M Na_2SO_4	147.2 (10 mV s^{-1}) 66.13 (0.5 A g^{-1})	29.38 (2.5 A g^{-1})	68.3% (1000 cycles)	…	…	99
rGO/MnO_2/PPy	3E	1 M Na_2SO_4	351 (0.5 A g^{-1})	268 (10 A g^{-1})	86% (1000 cycles)	…	…	38
GF@PPy@MnO_2	3E	1 M Na_2SO_4	601 (1 A g^{-1})	245 (50 A g^{-1})	92% (5000 cycles)	14	13000	40
rGO/MnO_2/PPy	3E	1 M H_2SO_4	366 (1 A g^{-1})	…	85% (3500 cycles)	7.64	2500	36
CNTs(rGO/MnO_2/PPy)	3E	2 M KCl	295.83 (0.5 A g^{-1})	…	86.15% (1000 cycles)	11.22	807.67	39
rGO/$ZnMn_2O_4$@PPy	3E	1 M Na_2SO_4	108.24 (0.2 A g^{-1})	70 (5 A g^{-1})	84.03% (5000 cycles)	-	-	100
MoO_3/PPy/rGO	3E	1 M Na_2SO_4	412.3 (0.5 A g^{-1})	107.3 (10 A g^{-1})	85.1% (6000 cycles)	19.8	301	101
TiO_2@PPy/rGO	3E	2 M KOH	410.1 (1 A g^{-1})	287.3 (5 A g^{-1})	%70 (1500 cycles)	-	-	102
rGO/$CoFe_2O_4$/PPy	2E	1 M H_2SO_4	164 (5 mV s^{-1})	…	…	22.8	410	103
rGO/MnO_2/PPy	2E	1 M H_2SO_4	285.91 (1 mV s^{-1})	…	94.7% (1000 cycles)	7.75	2845.7	34
rGO/MnO_2/PANI	2E	1 M Na_2SO_4	592 (1 A g^{-1})	249 (5 A g^{-1})	89% (6000 cycles)	…	…	104
rGO-$MnO_2$2-PPy16	**2E**	**1 M H_2SO_4**	**331.76 (20 mV s^{-1}) 220.16 (0.5 A g^{-1})**	**155.24 (20 A g^{-1})**	**86.08 % (5000 cycles)**	**6.19* 24.76****	**1512.8**	This work
		0.5 M Na_2SO_4	**475.6 (20 mV s^{-1}) 345.87 (0.5 A g^{-1})**	**177.04 (20 A g^{-1})**	**88.85 % (5000 cycles)**	**8.65* 34.6****	**1421.9**	

Bold values indicate the selected composite exhibiting the best electrochemical performance

* Energy density obtained from Eq. 3 for the symmetric two-electrode configuration.

** Energy density calculated based on electrode capacitance.

rGO-$MnO_2$2-PPy16 nanocomposite is promising electrode material for energy storage devices.

Conclusion

In this study, electrodes with high electrochemical performance were successfully developed using rGO-MnO_2-PPy ternary nanocomposites synthesized through *in situ* polymerization of pyrrole on the surface of hydrothermally synthesized rGO-MnO_2. The addition of MnO_2 increased the pseudocapacitive effect and specific capacitance; however, excessive MnO_2 loading limited the cycle life. The optimal composition was determined to be 2:1 ($KMnO_4$:rGO, m/m) and 1:16 (rGO-$MnO_2$2:Pyrrole, m/m). The addition of PPy to the composite increased conductivity, facilitating ion transport and further enhancing capacitance. The nanocomposite exhibited high performance in both acidic (H_2SO_4) and neutral (Na_2SO_4) electrolytes. Capacitance values of 331.76 F g^{-1} (20 mV s^{-1}) and 204.35 F g^{-1} (1 A g^{-1}) were

obtained in 1 M H_2SO_4 electrolyte, while values of 475.6 F g^{-1} and 323.91 F g^{-1} were obtained in 0.5 M Na_2SO_4 electrolyte. Furthermore, it was observed that the rGO-$MnO_2$2-PPy16 electrode exhibited excellent capacity retention rates of 88.85% and 86.08% for 5000 cycles at a current density of 10 A g^{-1} in Na_2SO_4 and H_2SO_4 electrolytes, respectively. The findings indicated that rGO-MnO_2-PPy nanocomposites are promising electrode materials for supercapacitors due to their electrochemical properties, including pronounced pseudocapacitive responses, enhanced charge transfer properties, and extended lifespan by adapting to different electrolyte environments.

Supplementary Information The online version contains supplementary material available at https://doi.org/10.1007/s11664-026-12965-0.

Acknowledgments The authors thank the Scientific and Technological Research Council of Türkiye (TÜBİTAK; Project No. 120M752). The authors gratefully acknowledge Dr. Hakan Eskizengin (Department of Biology, Ankara University) for his assistance with TEM imaging.

Funding Open access funding provided by the Scientific and Technological Research Council of Türkiye (TÜBİTAK).

Conflict of Interest The authors declare that they do not have any conflict of interest.

Open Access This article is licensed under a Creative Commons Attribution 4.0 International License, which permits use, sharing, adaptation, distribution and reproduction in any medium or format, as long as you give appropriate credit to the original author(s) and the source, provide a link to the Creative Commons licence, and indicate if changes were made. The images or other third party material in this article are included in the article's Creative Commons licence, unless indicated otherwise in a credit line to the material. If material is not included in the article's Creative Commons licence and your intended use is not permitted by statutory regulation or exceeds the permitted use, you will need to obtain permission directly from the copyright holder. To view a copy of this licence, visit http://creativecommons.org/licenses/by/4.0/.

References

1. L. Olatomiwa, H.O. Idakwo, W.S. Olusola, and C. Ezeh, Global energy consumption trends. *Majlesi J. Electr. Eng.* 19, 1 (2025).
2. E. Antolini, Composite materials: an emerging class of fuel cell catalyst supports. *Appl. Catal. B* 100, 413 (2010).
3. J. Bezuidenhout, J. Rens, B. Peterson, and G. Botha, Case where the general summation law underestimates the aggregation of voltage unbalance emission, In 2025 IEEE 15th International Workshop on Applied Measurements for Power Systems. (AMPS), 1
4. S. K. Gupta and K. Gandhi, Voltage issues in power networks with renewable power generation, In: Renewable Energy Integration to the Grid (CRC Press, 2022), 79
5. J. Pegueroles-Queralt, F.D. Bianchi, and O. Gomis-Bellmunt, A power smoothing system based on supercapacitors for renewable distributed generation. *IEEE Trans. Ind. Electron.* 62(1), 343 (2014).
6. M. H. Hasan, A. Roy, M. M. B. Sakib, A. Z. Rizve, A review of grid-connected supercapacitor systems, In: Proc. IEEE Int. Conf. Power Electr. Electron. Ind. Appl 993–998 (2024).
7. T. Ariyarathna, N. Kularatna, and D. A. Steyn-Rosse, Supercapacitor assisted hybrid DC-DC converter for applications powered by renewable energy sources, In: Proc. IEEE Int. Conf. Ind. Electron. Sustain. Energy Syst. (IESES) 194–199 (2020).
8. B. Pal, S. Yang, S. Ramesh, V. Thangadurai, and R. Jose, Electrolyte selection for supercapacitive devices: a critical review. *Nanoscale Adv.* 1(10), 3807 (2019).
9. I. Aldama, V. Barranco, M. Kunowsky, J. Ibañez, and J.M. Rojo, Contribution of cations and anions of aqueous electrolytes to the charge stored at the electric electrolyte/electrode interface of carbon-based supercapacitors. *J. Phys. Chem. C* 121(22), 12053 (2017).
10. C. Zhong, Y. Deng, W. Hu, J. Qiao, L. Zhang, and J. Zhang, A review of electrolyte materials and compositions for electrochemical supercapacitors. *Chem. Soc. Rev.* 44(21), 7484 (2015).
11. S. N. Pronkin, N. Y. Shokina, and C. Pham-Huu, Redox transitions in pseudocapacitor materials: criteria and ruling factors, In: Redox Chemistry—from Molecules to Energy Storage (2022).
12. V. Molahalli, K. Chaithrashree, M.K. Singh, M. Agrawal, S.G. Krishnan, and G. Hegde, Past decade of supercapacitor research-lessons learned for future innovations. *J. Energy Storage* 70, 108062 (2023).
13. H. Li, A review of EDLC and pseudocapacitance with synergistic integration of carbon-based and metal oxide materials for enhanced electrochemical energy storage. *Appl. Comput. Eng.* 61, 231 (2024).
14. Z.S. Iro, C. Subramani, and S.S. Dash, A brief review on electrode materials for supercapacitor. *Int. J. Electrochem. Sci.* 11(12), 10628 (2016).
15. S. Karthikeyan, B. Narenthiran, A. Sivanantham, L.D. Bhatlu, and T. Maridurai, Supercapacitor: evolution and review. *Mater. Today Proc.* 46, 3984 (2020).
16. G. Sriram, M. Arunpandian, K. Dhanabalan, V.R. Sarojamma, S. David, M.D. Kurkuri, and T.H. Oh, Recent progress using graphene oxide and its composites for supercapacitor applications: a review. *Inorganics* 12(6), 145 (2024).
17. S. Chen, W. Wang, X. Zhang, and X. Wang, High-performance supercapacitors based on graphene/activated carbon hybrid electrodes prepared via dry processing. *Batteries* 10(6), 195 (2024).
18. S. Rai, R. Bhujel, and B. P. Swain, Electrochemical analysis of graphene oxide and reduced graphene oxide for super capacitor applications, In: Proc. IEEE Electron Devices Kolkata Conf. (EDKCON), pp. 489–492 (2018).
19. A. C. Preethi, V. Hariharakrishnan, and V. Saraswathi, Electrochemical properties of GO–rGO: Insights from modified Hummers synthesis and thermal reduction (2024).
20. Y.P. Zhu, C. Xia, Y. Lei, N. Singh, U. Schwingenschlögl, and H.N. Alshareef, Solubility contrast strategy for enhancing intercalation pseudocapacitance in layered MnO2 electrodes. *Nano Energy* 56, 357 (2019).
21. S Lichchhavi AK Kumar Srivastava SK Jha Elucidation of intercalation-pseudocapacitor mechanism in Binder-free Bi2S3@Ni foam electrodes towards high-performance supercapattery Electrochim. Acta 456 142438 (2023).
22. A. Joseph, and T. Thomas, *Pseudocapacitance: An Introduction, in Pseudocapacitors* (Cham: Springer, 2024), pp.1–17.
23. M. Vangari, T. Pryor, and L. Jiang, Supercapacitors: review of materials and fabrication methods. *J. Energy Eng.* 139, 72 (2013).
24. M.E. Şahin, F. Blaabjerg, and A. Sangwongwanich, A comprehensive review on supercapacitor applications and developments. *Energies* 15(3), 674 (2022).

25. J. Liu, J. Bao, X. Zhang, Y. Gao, Y. Zhang, L. Liu, and Z. Cao, MnO2-based materials for supercapacitor electrodes: challenges, strategies and prospects. *RSC Adv.* 12(55), 35556 (2022).
26. D. Mondal, M. Kundu, B.K. Paul, D. Bhattacharya, S. Sarkar, S. Sau, D. Senapati, T.K. Mandal, and S. Das, Rare earth ion-doped α-MnO2 nanorods for an asymmetric supercapacitor. *ACS Appl. Nano Mater.* 7, 4913 (2024).
27. M. Diantoro, I. Istiqomah, Y.A. Fath, N. Nasikhudin, Y. Alias, and W. Meevasana, Potential of MnO2-based composite and numerous morphological for enhancing supercapacitors performance. *Int. J. Appl. Ceram. Technol.* 20(4), 2077 (2023).
28. S. Wang, W. Chen, X. Huang, X. Chen, D. Li, F. Yu, and Y. Chen, A free-standing polymer polypyrrole/cellulose composite film via spatial-confined interfacial electrodeposition for flexible supercapacitors. *Materials* 16(19), 6476 (2023).
29. P.S. Gaikar, K.S. Kadu, K.K. Tehare, G.C. Wadhawa, S.H. Mahmood, and T.L. Lambat, Recent developments in polypyrrole/manganese oxide-based nanocomposites for thin film electrodes in supercapacitors: A minireview. *Nanoscale Adv.* 4(24), 5245 (2022).
30. R. Yadav, A. Saini, J. Choudhary, S. Sardana, A. Ohlan, K. Singh, and S.P. Singh, High-performance flexible supercapacitor based on morphology tuned polypyrrole/molybdenum disulfide nanocomposites. *Energy Storage* 5, e477 (2023).
31. F.F. Sun, W.H. Li, Z.H. Huang, W. Sun, Y. Dou, D. Yuan, B. Jia, and T. Ma, Pulse-potential electrochemistry to boost real-life application of pseudocapacitive dual-doped polypyrrole. *SmartMat* 3, 644 (2022).
32. E. Pameté, L. Köps, F.A. Kreth, S. Pohlmann, A. Varzi, T. Brousse, A. Balducci, and V. Presser, The Many Deaths of Supercapacitors: Degradation, Aging, and Performance Fading. *Adv. Energy Mater.* 13(29), 2301008 (2023).
33. S.M. Alsufyani, R. Jafer, J. Iqbal, R. Alwafi, S. Bashir, S. Ramesh, and K. Ramesh, Carbon and polymer-based conducting platforms incorporated with electroactive metal-oxides/sulphides for energy storage devices. *J. Energy Storage* 84, 110713 (2024).
34. M. Ates, I. Mizrak, O. Kuzgun, and S. Aktas, Synthesis, characterization, and supercapacitor performances of activated and inactivated rGO/MnO2 and rGO/MnO2/PPy nanocomposites. *Ionics* 26, 4723 (2020).
35. S. Wang, N. Liu, J. Rao, Y. Yue, K. Gao, J. Su, L. Li, X. Jiang, Z. Liu, and Y. Gao, Vertical finger-like asymmetric supercapacitors for enhanced performance at high mass loading and inner integrated photodetecting systems. *J. Mater. Chem. A* 5, 22199 (2017).
36. P. Lv, X. Tang, J. Yuan, and C. Ji, Highly compressible reduced graphene oxide/polypyrrole/MnO2 aerogel electrodes meeting the requirement of limiting space. *Mater. Res. Express* 4, 115602 (2017).
37. G. Han, Y. Liu, E. Kan, J. Tang, L. Zhang, H. Wang, and W. Tang, Sandwich-structured MnO2/polypyrrole/reduced graphene oxide hybrid composites for high-performance supercapacitors. *RSC Adv.* 4, 9898 (2014).
38. H. Zhou, Z. Yan, X. Yang, J. Lv, L. Kang, and Z.-H. Liu, RGO/MnO2/polypyrrole ternary film electrode for supercapacitor. *Mater. Chem. Phys.* 177, 40 (2016).
39. S.A. El-Khodary, I.S. Yahia, H.Y. Zahran, and M. Ibrahim, Preparation of polypyrrole-decorated MnO2/reduced graphene oxide in the presence of multi-walled carbon nanotubes composite for high performance asymmetric supercapacitors. *Physica B Condens. Matter* 556, 66 (2019).
40. T. Qin, B. Liu, Y. Wen, Z. Wang, X. Jiang, Z. Wan, S. Peng, G. Cao, and D. He, Freestanding flexible graphene foams@polypyrrole@MnO2 electrodes for high-performance supercapacitors. *J. Mater. Chem. A* 4, 9196 (2016).
41. Y. Liu, C. Yu, X. Song, S. Hou, S. Lan, J. Yu, Y. Xie, and J. Qiu, An effective 'salt in dimethyl sulfoxide/water' electrolyte enables high-voltage supercapacitor operated at −50°C. *J. Energy Chem.* 93, 361 (2024).
42. T. Le, Y. Yang, L. Yu, Z. Huang, and F. Kang, In-situ growth of MnO2 crystals under nanopore-constraint in carbon nanofibers and their electrochemical performance. *Sci. Rep.* 6, 37368 (2016).
43. D. Wu et al., Hybrid MnO2/C nano-composites on a macroporous electrically conductive network for supercapacitor electrodes. *J. Mater. Chem. A* 3, 16695 (2015).
44. Q. Yang, L. Dong, C. Xu, and F. Kang, High-performance supercapacitors based on graphene/MnO2/activated carbon fiber felt composite electrodes in different neutral electrolytes. *RSC Adv.* 6, 12525 (2016).
45. M. Yu, D. Lin, H. Feng, Y. Zeng, Y. Tong, and X. Lu, Boosting the energy density of carbon-based aqueous supercapacitors by optimizing the surface charge. *Angew. Chem.* 129, 5546 (2017).
46. K. An, J. He, L. Yang, L. Shen, and Y. Sun, Facile synthesis of loosely assembled α-MnO2 nanofiber coated with GQD/PANI for enhancing capacity. *Int. J. Energy Res.* 44, 12180 (2020).
47. Z. Çıplak, and N. Yıldız, A parametric study for the synthesis of graphene–AgAu nanocomposites: performances as electrode material. *J. Mater. Sci. Mater. Electron.* 29, 10411 (2018).
48. C. Huang, Y. Ding, C. Hao, S. Zhou, X. Wang, H. Gao, L. Zhu, and J. Wu, PVP-assisted growth of Ni-Co oxide on N-doped reduced graphene oxide with enhanced pseudocapacitive behavior. *Chem. Eng. J.* 378, 122202 (2019).
49. B. Getiren, H. Altınışık, Z. Çıplak, F. Soysal, and N. Yıldız, Nitrogen-doped graphene quantum dots/co-doped PANI binary nanocomposites as high-performance supercapacitor electrode materials. *Synth. Met.* 298, 117451 (2023).
50. V. Hoseinpour, M. Souri, and N. Ghaemi, Green synthesis, characterisation, and photocatalytic activity of manganese dioxide nanoparticles. *Micro Nano Lett.* 13, 1560 (2018).
51. A. Kumar, M.S. Aathira, U. Pal, and S.L. Jain, Photochemical oxidative coupling of 2-naphthols using a hybrid reduced graphene oxide/manganese dioxide nanocomposite under visible-light irradiation. *ChemCatChem* 10, 1844 (2018).
52. A. Aleena, A. Asadullah, A. Khan, M. Humayun, N. Shah, M. Bououdina, A.F. Alanazi, and A. Iqbal, MnO2-decorated rGO: a functional material for Congo Red dye removal. *Green Chem. Lett. Rev.* 18, 2542391 (2025).
53. V. Janakiraman, M. Varun, G.S. Uthayakumar, V. Loganathan, G. Kalpanadevi, and J. Navarajan, Synthesis of MnO2@2D rGO hybrid nanocomposite for efficient removal of hazardous textile dyes from water. *Ionics* 31, 6527 (2025).
54. J. Nayak, S. K. Mahadeva, J. Kim, Characteristics of flexible electrode made on cellulose by soluble polypyrrole coating. Proc. Inst. Mech. Eng. C J. Mech. Eng. Sci. **226**, 2605 (2012).
55. S. Maruthamuthu, J. Chandrasekaran, D. Manoharan, and R. Magesh, Conductivity and dielectric analysis of nanocolloidal polypyrrole particles functionalized with higher weight percentage of poly(styrene sulfonate) using the dispersion polymerization method. *J. Polym. Eng.* 37, 481 (2017).
56. H. Wang, Z. Lu, D. Qian, Y. Li, and W. Zhang, Single-crystal α-MnO2 nanorods: Synthesis and electrochemical properties. *Nanotechnology* 18, 115616 (2007).
57. T.S. Munonde, A. Nqombolo, S. Hobongwana, A. Mpupa, and P.N. Nomngongo, Removal of methylene blue using MnO2@rGO nanocomposite from textile wastewater: Isotherms, kinetics and thermodynamics studies. *Heliyon* 9, e15502 (2023).
58. S. Sivakumar, D. Subramanian, P. Sengodan, R. Rajendran, and G. Raju, Facile synthesis and characterization of MnO2/

MWCNT nanocomposites for high-performance asymmetric supercapacitor. *Ionics* 28, 3975 (2022).
59. T. Bashir, A. Shakoor, E. Ahmed, N. A. Niaz, M. Saeed Akhtar, M. R. Raza, M. A. Malik, and P. J. S. Foot, Polypyrrole-Fe2O3 nanocomposites with high dielectric constant: *In situ* chemical polymerisation 26 233 (2018).
60. B. Getiren, Z. Çıplak, C. Gökalp, and N. Yıldız, Novel approach in synthesizing ternary GO-Fe3O4-PPy nanocomposites for high photothermal performance. *J. Appl. Polym. Sci.* 137, 48837 (2020).
61. Z. Li, H. Liu, H. Ruan, R. Hu, Y. Su, Z. Hu, and J. Huang, *In situ* synthesis rodlike MnO2/reduced graphene oxide composite as anode materials for Li-ion batteries. *J. Mater. Sci. Mater. Electron.* 28, 18099 (2017).
62. R.A. Davoglio, G. Cabello, J.F. Marco, and S.R. Biaggio, Synthesis and characterization of α-MnO2 nanoneedles for electrochemical supercapacitors. *Electrochim. Acta* 261, 428 (2018).
63. M. Gayathri, S. Rajesh, and E. Sundaravadivel, Synthesis of MnO2/g-C3N4 nanocomposite for the efficient photocatalytic degradation of methylene blue and acid blue 113 dyes. *J. Mater. Sci. Mater. Electron.* 35, 1858 (2024).
64. Z. Yang, Z. Tian, and C. Qi, Ru nanoclusters on MnO2 nanotubes for boosting electrochemical nonenzymatic H2O2 sensing. *ACS Appl. Nano Mater.* 6, 21141 (2023).
65. S. Kulandaivalu, M. Z. Hussein, A. Mohamad Jaafar, M. A. A. Mohd Abdah, N. H. N. Azman, and Y. Sulaiman, A simple strategy to prepare a layer-by-layer assembled composite of Ni–Co LDHs on polypyrrole/rGO for a high specific capacitance supercapacitor. RSC Adv. **9**, 40478 (2019).
66. F. Liang, Z. Liu, and Y. Liu, Enhanced electrochemical properties of MnO2/PPy nanocomposites by miniemulsion polymerization. *J. Mater. Sci. Mater. Electron.* 28, 10603 (2017).
67. M. Thommes, K. Kaneko, A.V. Neimark, J.P. Olivier, F. Rodriguez-Reinoso, J. Rouquerol, and K.S.W. Sing, Physisorption of gases, with special reference to the evaluation of surface area and pore size distribution (IUPAC Technical Report). *Pure Appl. Chem.* 87, 1051 (2015).
68. S.W. Lee, S.M. Bak, C.W. Lee, C. Jaye, D.A. Fischer, B.K. Kim, X.Q. Yang, K.W. Nam, and K.B. Kim, Structural changes in reduced graphene oxide upon MnO2 deposition by the redox reaction between carbon and permanganate ions. *J. Phys. Chem. C* 118, 2834 (2014).
69. Y. Chen, X. Zhang, D. Zhang, P. Yu, and Y. Ma, High performance supercapacitors based on reduced graphene oxide in aqueous and ionic liquid electrolytes. *Carbon N. Y.* 49, 573 (2011).
70. J. Yan, J. Liu, Z. Fan, T. Wei, and L. Zhang, High-performance supercapacitor electrodes based on highly corrugated graphene sheets. *Carbon N. Y.* 50, 2179 (2012).
71. M. Xu, L. Kong, W. Zhou, and H. Li, Hydrothermal synthesis and pseudocapacitance properties of α-MnO2 hollow spheres and hollow urchins. *J. Phys. Chem. C* 111, 19141 (2007).
72. L. Zhang, X. Hu, Z. Wang, F. Sun, and D.G. Dorrell, A review of supercapacitor modeling, estimation, and applications: A control/management perspective. *Renew. Sustain. Energy Rev.* 81, 1868 (2018).
73. S. Sahoo, S. Dhibar, and C.K. Das, Facile synthesis of polypyrrole nanofiber and its enhanced electrochemical performances in different electrolytes. *Express Polym Lett* 6, 965 (2012).
74. A.A. Iurchenkova, T. Kallio, and E.O. Fedorovskaya, Relationships between polypyrrole synthesis conditions, its morphology and electronic structure with supercapacitor properties measured in electrolytes with different ions and pH values. *Electrochim. Acta* 391, 138892 (2021).
75. A.C. Lazanas, and M.I. Prodromidis, Electrochemical impedance spectroscopy—a tutorial. *ACS Meas. Sci. Au* 3(3), 162 (2023).
76. NHN Azman MS Mamat Mat Nazir LH Ngee Y Sulaiman Graphene-based ternary composites for supercapacitors Int. J. Energy Res. **42** 6 2104 (2018).
77. H. Bian and Y. Zhang, An Equivalent Circuit for Describing the Electrochemical Impedance Spectroscopy Spectra of Lithium-Ion Battery Porous Electrode. ECS Meet. Abstr. MA2014-03, 53 (2014).
78. S. Khan, S. A. Rizvi, and S. Urooj, Equivalent circuit modelling using electrochemical impedance spectroscopy for different materials of SOFC, In: Proc. Int. Conf. Comput. Sustain. Glob. Dev. (INDIACom), pp. 1563–1567 (2016).
79. K. Mazloomian, H.J. Lancaster, C.A. Howard, P.R. Shearing, and T.S. Miller, Supercapacitor Degradation: Understanding Mechanisms of Cycling-Induced Deterioration and Failure of a Pseudocapacitor. *Batter. Supercaps* 6, 202300214 (2023).
80. X. Chen, Y. Wu, and R. Holze, Ag(e)ing and degradation of supercapacitors: Causes, mechanisms, models and countermeasures. *Molecules* 28(13), 5028 (2023).
81. C.J. Raj, M. Rajesh, R. Manikandan, S. Park, J.H. Park, K.H. Yu, and B.C. Kim, Electrochemical impedance spectroscopic studies on aging-dependent electrochemical degradation of p-toluene sulfonic acid-doped polypyrrole thin film. *Ionics (Kiel).* 24(8), 2335–2342 (2018).
82. W.K. Chee, H.N. Lim, I. Harrison, K.F. Chong, Z. Zainal, C.H. Ng, and N.M. Huang, Performance of Flexible and Binderless Polypyrrole/Graphene Oxide/Zinc Oxide Supercapacitor Electrode in a Symmetrical Two-Electrode Configuration. *Electrochim. Acta* 157, 88 (2015).
83. J. Xue, Q. Yang, R. Guan, Q. Shen, X. Liu, H. Jia, and Q. Li, High-performance ordered porous Polypyrrole/ZnO films with improved specific capacitance for supercapacitors. *Mater. Chem. Phys.* 256, 123593 (2020).
84. J. Wang, Y. Xu, J. Zhu, and P. Ren, Electrochemical *in situ* polymerization of reduced graphene oxide/polypyrrole composite with high power density. *J. Power. Sources* 208, 138 (2012).
85. H. Feng, B. Wang, L. Tan, N. Chen, N. Wang, and B. Chen, Polypyrrole/hexadecylpyridinium chloride-modified graphite oxide composites: Fabrication, characterization, and application in supercapacitors. *J. Power. Sources* 246, 621 (2014).
86. B.M. Hryniewicz, I.C. Gil, and M. Vidotti, Enhancement of polypyrrole nanotubes stability by gold nanoparticles for the construction of flexible solid-state supercapacitors. *J. Electroanal. Chem.* 911, 116212 (2022).
87. M. Ates, and Y. Yuruk, Modelling of GO/PPy/CB and rGO/PPy/CB nanocomposite supercapacitors using an electrical equivalent circuit. *Ionics* 27, 4531 (2021).
88. K. Baruah, D. Sarmah, and A. Kumar, Ternary hybrid nanocomposites of polypyrrole nanotubes with 2D self-assembled heterostructures of protonated g-C3N4-rGO as supercapacitor electrodes. *Ionics (Kiel).* 27(7), 3153 (2021).
89. J. Zhu, Y. Xu, J. Wang, J. Wang, Y. Bai, and X. Du, Morphology controllable nano-sheet polypyrrole-graphene composites for high-rate supercapacitor. *Phys. Chem. Chem. Phys.* 17, 19885 (2015).
90. Z. Wang, P. Tammela, M. Strømme, and L. Nyholm, Nanocellulose coupled flexible polypyrrole@graphene oxide composite paper electrodes with high volumetric capacitance. *Nanoscale* 7, 3418 (2015).
91. R. Tas, H. Dunya, M. Gulen, and K. E. Karaoglanli, PPy@MWCNT nanocomposite for supercapacitor applications (2023)
92. S. S. Patil, V. L. Patil, A. K. Tawade, K. K. Sharma, A. G. Bhosale, S. A. Vhanalkar, (2023) Synthesis of MnO2 electrode material by electro-deposition method for the enhanced capacitive properties https://doi.org/10.21203/rs.3.rs-3056383/v1
93. Z. Wang, H. Wang, D. Pei, S. Wan, Z. Fan, M. Yu, and H. Lu, Refinement of structural characteristics and supercapacitor

performance of MnO2 nanosheets via CTAB-assisted electrodeposition. *Prog. Nat. Sci. Mater. Int.* 33, 881 (2023).
94. R.M. Obodo, H.E. Nsude, C.U. Eze, B.O. Okereke, S.C. Ezugwu, I. Ahmad, M. Maaza, and F.I. Ezema, Optimization of MnO2, NiO and MnO2@NiO electrodes using graphene oxide for supercapacitor applications. *Curr. Res. Green Sustain. Chem.* 5, 100345 (2022).
95. S. Abraham, M. Agnel, M.M. Antoinette, and S.P. Jose, One-step electrodeposition of lead oxide doped-polypyrrole for 3D high performance supercapacitors, in AIP Conf. *Proc.* 2369, 020118 (2021).
96. H. Lee, N. Noor, C. Gumeci, and D. Higgins, One-Pot Synthesis of MnO2/Reduced Graphene Oxide Via Hydrothermal Routes for Supercapacitor Applications. ECS Meet. Abstr. MA2022-01 **38**, 1686 (2022).
97. Y.-T. Weng, T.-Y. Huang, J.-F. Lee, H.-S. Sheu, and N.-L. Wu, Enhanced Performance of TiO2 Based Supercapacitor by MnO2 Modification. ECS Meet. Abstr. MA2015-02, **228** 558 (2015).
98. Y.C. Eeu, H.N. Lim, Y.S. Lim, S.A. Zakarya, and N.M. Huang, Electrodeposition of polypyrrole/reduced graphene oxide/iron oxide nanocomposite as supercapacitor electrode material. *J. Nanomater.* 2013(1), 653890 (2013).
99. T.V. Thu, T. Van Nguyen, X.D. Le, T.S. Le, V. Van Thuy, T.Q. Huy, and Q.D. Truong, Graphene-MnFe2O4-polypyrrole ternary hybrids with synergistic effect for supercapacitor electrode. *Electrochim. Acta* 314, 151–160 (2019).
100. Q.B. Le, E. Vargun, H. Fei, Q. Cheng, C. Bubulinca, R. Moučka, I. Sapurina, T.D. Tran, N.E. Kazantseva, and P. Saha, Effect of PANI and PPy on electrochemical performance of rGO/ZnMn2O4 aerogels as electrodes for supercapacitors. *J. Electron. Mater.* 49(8), 4697 (2020).
101. H. Deng, J. Huang, Z. Hu, X. Chen, D. Huang, and T. Jin, Fabrication of a three-dimensionally networked MoO3/PPy/rGO composite for a high-performance symmetric supercapacitor. *ACS Omega* 6(14), 9426 (2021).
102. S. Li, L. Zhang, L. Zhang, J. Zhang, H. Zhou, X. Chen, and T. Tang, The *in situ* construction of three-dimensional core–shell-structured TiO2@PPy/rGO nanocomposites for improved supercapacitor electrode performance. *New J. Chem.* 45(2), 1092 (2021).
103. S. Ishaq, M. Moussa, F. Kanwal, R. Ayub, T.N. Van, U. Azhar, and D. Losic, One step strategy for reduced graphene oxide/cobalt-iron oxide/polypyrrole nanocomposite preparation for high performance supercapacitor electrodes. *Electrochim. Acta* 427, 140883 (2022).
104. P.H. Wadekar, R.V. Khose, D.A. Pethsangave, and S. Some, One-step preparation of conducting polymer/metal oxide doped RGO trinary composite for supercapacitor applications. *ChemistrySelect* 5(38), 11769 (2020).

Publisher's Note Springer Nature remains neutral with regard to jurisdictional claims in published maps and institutional affiliations.

Authors and Affiliations

Beray Alyakut[1] · Zafer Çıplak[2] · Nuray Yıldız[3]

✉ Nuray Yıldız
nyildiz@eng.ankara.edu.tr

[1] Department of Chemical Engineering, Faculty of Engineering and Architecture, Eskişehir Osmangazi University, 26040 Eskişehir, Turkey

[2] Department of Chemical Engineering, Faculty of Engineering, Sivas Cumhuriyet University, 58140 Sivas, Turkey

[3] Department of Chemical Engineering, Faculty of Engineering, Ankara University, 06100 Ankara, Turkey